An updated hypoplastic model, its implementation and its application in tunnelling

A thesis for the doctor degree submitted to
University of Natural Resources and Applied Life Sciences, Vienna

submitted by

Xue-tao Wang, MSc

under the supervision of

Prof. Dr.-Ing. Wei Wu

Institute of Geotechnical Engineering
Department of Civil Engineering and Natural Hazards

Nr. 23

June 2009

Foreword of supervisor

Soil usually exhibits nonlinear behaviour at small strain and plastic behaviour at large strain. In design practice, however, elastic and perfectly plastic constitutive models are often used. Numerical analysis in tunnel design is largely based on the perfectly plastic Mohr-Coulomb model. The consideration of nonlinearity at small strain is but exception in practice. This thesis presents a significant improvement to settlement analysis of NATM tunnel by using an updated hypoplastic constitutive model. The hypoplastic model accounts for the nonlinear deformation at small strain and is simple enough to be applied in design practice. The five parameters can be easily determined by routine laboratory tests. The model is implemented into the commercial software FLAC3D. The implementation is verified by simulating various element tests and some benchmark problems. Finally, the settlement behaviour of a NATM tunnel under construction is studied using the hypoplastic model.

The development of constitutive models, the numerical implementation and the numerical simulation of complex excavation and support schemes pose a high challenge, which has been mastered successfully. Benefited from the interface provided by FLAC3D, the hypoplastic model runs as efficiently as the built-in models. We will use the hypoplastic model to solve other boundary value problems. The Otto Pregl Foundation for Geotechnical Fundamental Research is acknowledged for the financial support.

Acknowledgments

The thesis would not have been written in this form without the supervision and encouragement from Prof. Wu. He introduced me into numerical modelling in geomechanics and through our numerous discussions guided my research activities, particularly, managed to create perfect conditions for research.

I was lucky to work with many wise people who all left their traces in my research presented in this thesis.

Many thanks are due to all my colleagues and friends at our institute, who give me much help during my research work. I like to thank Mr. Josef Bauer for compiling the instrumentation data of Lainzer tunnel. Prof. Bauer from Graz Technical University is acknowleged for serving as the second examiner.

The author wishes to thank the Otto Pregl Foundation for Geotechnical Fundamental Research for the financial support.

My deep thank is also due to all my friends who help me adapt to live in Austria.

Finally, I express private gratitude to my parents, my brothers and sisters for their support throughout my entire studies. Even if thounds kilometers separate us, they always encourage me by their love.

Abstract

A new version of hypoplastic constitutive model is presented based on a specific constitutive equation by Wu and Bauer (1994). The failure surface and flow rule of the updated model is discussed and the calibration procedure of parameters is provided. The updated hypoplastic constitutive equation is implemented in the finite difference program FLAC3D. The implementation of hypoplastic constitutive model is verified by simulating some element tests e.g. isotropic compression test, triaxial test, biaxial test and simple shear test. Moreover, the excavation of a shallow tunnel with circular cross section is investigated. The influence of some model parameters on the surface settlement is studied. Then, the model performance is verified against a benchmark problem of a shallow tunnel from FLAC3D handbook. The numerical results are compared with those of the Mohr-Coulomb model. The longitudinal settlement agrees well with those of the Mohr-Coulomb model, while the transverse settlement troughs predicted by hypoplastic model are somewhat wider than those predicted by the Mohr-Coulomb model. Finally, the hypoplastic model is used for the numerical analyses of the Lainzer tunnel in Vienna, which is being currently constructed according the New Austrian Tunnelling Method (NATM). Besides the conventional support measures, advancing face support by horizontal glass fibre anchors is used. The influence of anchors on surface settlement is studied. The numerical results using the hypoplastic model are compared with the instrumentation data from site.

Zusammenfassung

Die vorliegende Arbeit beschäftigt sich mit der Entwicklung eines hypoplastischen Stoffgesetzes für Böden, die numerische Implementation in FLAC3D und die Anwendung auf seicht liegende Tunnel. Zunächst wurde das neue Stoffgesetz und das Kalibrierungsverfahren für die Modellparameter vorgestellt. Das neue Stoffgesetz wurde in FLAC3D implementiert. Das Stoffgsetz wurde durch die numerische Simulation von Elementversuchen, z.B. isotroper Kompressionsversuch, Triaxialversuch, Biaxialversuch und einfacher Scherversuch verifiziert. Darüberhinaus wurde der Ausbruch eines Hohlraums mit Kreisquerschnitt simuliert. Unser Hauptaugenmerk galt dem Setzungsverhalten. Der Einfluss der Modellparameter auf die Oberflächensetzungen wurde durch Parameterstudien untersucht. Ferner wurde unser Stoffgesetz anhand eines Beispiels aus FLAC3D-Handbuch verifiziert. Es handelt sich um Ausbruch und Sicherung eines seichten Tunnels mit vorauseilender Sicherung. Die numerischen Ergebnisse wurden mit denen des Mohr-Coulomb-Modells verglichen. Zum Schluß wurde Ausbruch und Sicherung des Lainzer Tunnels in Wien unterscuht. Der Lainzer-Tunnel wird zur Zeit nach der Neuen Österreichischen Tunnellbau Methode (NATM) gebaut. Außer den herkömmlichen Sicherungsmitteln wurden lange horizontale Glasfaseranker zur Sicherung der Ortsbrust und zur Minimierung der Setzung angesetzt. Der aufwendige Ulmenstollenvortrieb wurde durch umfangreiche 3D-Berechnungen realistisch simuliert. Der Einfluss der Horizontalanker auf die Oberflächn Setzungen wurde untersucht und mit den aus der Baustelle erhaltenen Messdaten verglichen.

Contents

Chapter 1

Introduction

Nowadays, numerical analysis becomes widely used in geotechnical engineering. With the rapid development of computer capacity, complicated geotechnical problems can be simulated more realistically, for example tunnelling. Depending on the method of excavation and support, tunnelling may induce considerable deformation to the surrounding ground. Consequently, in numerical simulation of tunnelling, a realistic ground model is crucial in order to estimate the magnitudes and distribution of the deformation.

The constitutive model frequently used in the numerical analysis of tunnelling is linear-elastic perfectly plastic with Mohr-Coulomb failure criterion. Numerous studies have shown that the use of such a constitutive model leads to shallower and wider settlement troughs than those observed. Recently, different material models for soil and its impact to numerical simulations of tunnelling have been studied. Some of those models are very simple to implement, while others are rather complicate and require many parameters, which are not easy to be determined. This study uses a constitutive model called hypoplastic model. The outstanding feature of hypoplastic constitutive model is its simplicity. The present thesis is intended to implement an updated hypoplastic constitutive model into a finite difference program, which is widely used in numerical analysis of geotechnical engineering. The numerical implementation is verified by simulating some laboratory experiments and then used to simulate some geotechnical problems. This thesis is organised as follows.

Chapter 2: This chapter overviews the develop history of hypoplasticity and presents a specific hypoplastic constitutive equation which is provided by Wu and Bauer (1994). A new hypoplastic constitutive equation is updated based on it. Some features of the updated model are discussed. The calibration procedure to obtain parameters for the hypoplastic constitutive model is provided.

Chapter 3: This chapter describes the theory and background of the explicit finite difference program ′FLAC3D′. The updated hypoplastic constitutive model is implemented into FLAC3D. The implemented hypoplastic constitutive model is verified and used to simulate some element tests in laboratory.

Chapter 4: The influences of the parameters of the hypoplastic constitutive model are studied in this chapter. Then the excavation and support for a shallow tunnel is simulated. The numerical results using the hypoplastic model are compared with the numerical results using the Mohr-Coulomb model.

Chapter 5: In this chapter, a tunnel constructed according to New Austrian Tunnelling Method is simulated using hypoplastic constitutive model in FLAC3D. This tunnel used a special advancing reinforcement by horizontal glass fibre anchors (GFK) besides the conventional support measurements. For testing the new method, a trial field was established in the project, where geotechnical instrumentation was carried out. The numerical results are compared with the measurements from this trial field.

Chapter 6: In this chapter, the work of the present thesis is summarized. Some conclusions are made and some recommendations for future research are given.

Chapter 2

Hypoplastic constitutive model

2.1 Introduction

The basic idea of hypoplasticity was developed by Kolymbas (1985) [8]. He formulated the behavior of anelasic material by using a nonlinear tensorial function of the rate-type. Hypoplasticity aims to describe the anelastic phenomena without using the notions introduced by elastoplasticity (such as yield surface, plastic potential ect.). Hypoplasticity recognizes that anelastic deformations may set on from the very beginning of the loading process. It does not presumptively distinguish between elastic and plastic deformations. The outstanding feature of hypoplasticity is its simplicity: it uses only a single equation (contrary to elastoplasticity) which holds equally for loading and unloading. As with every constitutive equation, there are several versions of hypoplastic equations, early ones and more advanced ones. The original hypoplastic equation given by Kolymbas (1977) [7], called generalized hypoelastic model, was too complex. Later some improved versions have been presented ([9], [11], [17], [22], [24]). The general hypoplastic constitutive equation was presented by Wu and Kolymbas (1990) [24]. Based on the general hypoplastic constitutive equation, a simple hypoplastic constitutive model was proposed by Wu (1999) [21]. However, this model shows excessive contraction (volume reduction). We proceed to update this constitutive model by including a new term into the model.

2.2 Framework of Hypoplasticity

The formal definition of hypoplasticity is provided by Wu and Kolymbas (1990)[24] as follows:

$$\mathring{\boldsymbol{\sigma}} = \mathbf{H}(\boldsymbol{\sigma}, \dot{\boldsymbol{\epsilon}}) \tag{2.1}$$

where $\mathring{\boldsymbol{\sigma}}$ is the Jaumann stress rate defined as

$$\mathring{\boldsymbol{\sigma}} = \dot{\boldsymbol{\sigma}} + \boldsymbol{\sigma}\dot{\boldsymbol{\omega}} - \dot{\boldsymbol{\omega}}\boldsymbol{\sigma} \tag{2.2}$$

where $\dot{\boldsymbol{\sigma}}$ is the time derivative of the Cauchy stress $\boldsymbol{\sigma}$, and $\dot{\boldsymbol{\omega}}$ is the rotation rate (spin tensor). Furthermore, the function in equation (2.1) is required to be not differentiable in and only in $\dot{\boldsymbol{\epsilon}} = \mathbf{0}$.

To obtain a concrete formulation, some restrictions are imposed on the constitutive equation (2.1). Some of the restrictions are based on the general principles of continuum mechanics, while others are based on experimental observations. The behaviour to be described is assumed to be rate-independent. These restrictions are described as follows:

1. The function $\mathbf{H}$ should be positively homogeneous of the first order in

   $$\mathbf{H}(\boldsymbol{\sigma}, \lambda\dot{\boldsymbol{\epsilon}}) = \lambda\mathbf{H}(\boldsymbol{\sigma}, \dot{\boldsymbol{\epsilon}}) \tag{2.3}$$

   where λ is a positive but otherwise arbitrary scalar.

2. The function $\mathbf{H}$ should fulfill the following condition of objectivity

   $$\mathbf{H}(\mathbf{Q}\boldsymbol{\sigma}\mathbf{Q}^T, \mathbf{Q}\dot{\boldsymbol{\epsilon}}\mathbf{Q}^{\mathrm{T}}) = \mathbf{Q}\mathbf{H}(\boldsymbol{\sigma}, \dot{\boldsymbol{\epsilon}})\mathbf{Q}^{\mathrm{T}} \tag{2.4}$$

   where $\mathbf{Q}$ is an orthogonal tensor. The representation theorem for a tensorial function of two symmetric tensors can be written as follows ([5])

   $$\begin{aligned}\mathring{\boldsymbol{\sigma}} = {} & \alpha_0\mathbf{1} + \alpha_1\boldsymbol{\sigma} + \alpha_2\dot{\boldsymbol{\epsilon}} + \alpha_3\boldsymbol{\sigma}_2 + \alpha_4\dot{\boldsymbol{\epsilon}}_2 + \alpha_5(\boldsymbol{\sigma}\dot{\boldsymbol{\epsilon}} + \dot{\boldsymbol{\epsilon}}\boldsymbol{\sigma}) + \\ & \alpha_6(\boldsymbol{\sigma}_2\dot{\boldsymbol{\epsilon}} + \dot{\boldsymbol{\epsilon}}\boldsymbol{\sigma}_2) + \alpha_7(\boldsymbol{\sigma}\dot{\boldsymbol{\epsilon}}_2 + \dot{\boldsymbol{\epsilon}}_2\boldsymbol{\sigma}) + \alpha_8(\boldsymbol{\sigma}_2\dot{\boldsymbol{\epsilon}}_2 + \dot{\boldsymbol{\epsilon}}_2\boldsymbol{\sigma}_2)\end{aligned} \tag{2.5}$$

   where $\mathbf{1}$ is the unit tensor. The coefficient $\alpha_i (i = 0, \cdots, 8)$ are the function of the invariants and joint invariants of $\boldsymbol{\sigma}$ and $\dot{\boldsymbol{\epsilon}}$

$$\begin{aligned}\alpha_i = \alpha_i(&\mathrm{tr}\boldsymbol{\sigma}, \mathrm{tr}\boldsymbol{\sigma}_2, \mathrm{tr}\boldsymbol{\sigma}_3, \mathrm{tr}\dot{\boldsymbol{\epsilon}}, \mathrm{tr}\dot{\boldsymbol{\epsilon}}_2, \mathrm{tr}\dot{\boldsymbol{\epsilon}}_3,\\ &\mathrm{tr}(\boldsymbol{\sigma}\dot{\boldsymbol{\epsilon}}), \mathrm{tr}(\boldsymbol{\sigma}_2\dot{\boldsymbol{\epsilon}}), \mathrm{tr}(\boldsymbol{\sigma}\dot{\boldsymbol{\epsilon}}_2), \mathrm{tr}(\boldsymbol{\sigma}_2\dot{\boldsymbol{\epsilon}}_2))\end{aligned} \tag{2.6}$$

where tr represents the trace of a tensor. Note that the isotropy of the tensorial function does not necessarily mean that the response is also isotropic.

3. The function H should be homogeneous in $\boldsymbol{\sigma}$, i.e.

$$\mathbf{H}(\boldsymbol{\sigma}, \lambda\dot{\boldsymbol{\epsilon}}) = \lambda^n \mathbf{H}(\boldsymbol{\sigma}, \dot{\boldsymbol{\epsilon}}) \tag{2.7}$$

   where λ denotes an arbitrary scalar and n denotes the order of homogeneity. This restriction implies that the tangential stiffness is proportional to the nth power if the stress level $(\mathrm{tr}\boldsymbol{\sigma})^n$, so that experiments conducted under different stress levels can be normalized by $(\mathrm{tr}\boldsymbol{\sigma})^n$.

Without loss in generality, it is assumed that the constitutive equation can be decomposed into two parts representing reversible and irreversible behaviour of the material:

$$\mathring{\boldsymbol{\sigma}} = \mathbf{L}(\boldsymbol{\sigma}, \dot{\boldsymbol{\epsilon}}) - \mathbf{N}(\boldsymbol{\sigma}, \dot{\boldsymbol{\epsilon}}) \tag{2.8}$$

where $\mathbf{L}$ is assumed to be linear in $\dot{\boldsymbol{\epsilon}}$ and $\mathbf{N}$ is non-linear in $\dot{\boldsymbol{\epsilon}}$. $\mathbf{L}(\boldsymbol{\sigma}, \dot{\boldsymbol{\epsilon}})$ in equation (2.8) can be specified by invoking the representation theorem for isotropic tensorial functions, and the non-linear dependence of $\mathbf{N}$ on $\dot{\boldsymbol{\epsilon}}$ should also satisfy the restriction of rate-independence. Furthermore, the following generalized hypoplastic equation could be assumed ([25])

$$\mathring{\boldsymbol{\sigma}} = \mathsf{L}(\boldsymbol{\sigma}) : \dot{\boldsymbol{\epsilon}} - \mathbf{N}(\boldsymbol{\sigma})\|\dot{\boldsymbol{\epsilon}}\| \tag{2.9}$$

where $\mathsf{L} = \partial\mathbf{L}/\partial\dot{\boldsymbol{\epsilon}}$ is, in analogy to the elastic stiffness matrix, a fourth-order tensor. $\|\dot{\boldsymbol{\epsilon}}\| = \sqrt{\mathrm{tr}\dot{\boldsymbol{\epsilon}}^2}$ stands for the Euclidean norm. The colon : denotes an inner product between two tensors.

It should be noticed that equation (2.9) can describe the relationship of stress rates and strain rates without any predefined yield surface and plastic potential. Another advantage of this hypoplastic model is the fact that the decomposition of elastic and plastic parts is not used in developing the constitutive equation. Moreover, there is even no need to define loading and unloading explicitly, since they are implied by the constitutive equation.

2.3 Implementation of hypoplastic model by Wu

2.3.1 A simple hypoplastic constitutive equation

The following constitutive equation was proposed by Wu (1992) [20]:

$$\overset{\circ}{\boldsymbol{\sigma}} = \mathrm{c}_1(\mathrm{tr}\boldsymbol{\sigma})\dot{\boldsymbol{\epsilon}} + \mathrm{c}_2\frac{\mathrm{tr}(\boldsymbol{\sigma}\dot{\boldsymbol{\epsilon}})}{\mathrm{tr}\boldsymbol{\sigma}}\boldsymbol{\sigma} + \Big(\mathrm{c}_3\frac{\boldsymbol{\sigma}^2}{\mathrm{tr}\boldsymbol{\sigma}} + \mathrm{c}_4\frac{\boldsymbol{\sigma}^{*2}}{\mathrm{tr}\boldsymbol{\sigma}}\Big)\|\dot{\boldsymbol{\epsilon}}\| \tag{2.10}$$

where c_i, $(i = 1, 2, 3, 4)$ are dimensionless parameters. The deviatoric stress tensor $\boldsymbol{\sigma}^*$ in the above equation is given by $\boldsymbol{\sigma}^* = \boldsymbol{\sigma} - 1/3(\mathrm{tr}\boldsymbol{\sigma})\mathbf{1}$. The four parameters can be identified with a single triaxial compression test. The performance of the model was shown in great detail by Wu and Bauer (1994).

2.3.2 Calibration procedure of parameters

The calibration procedure of four parameters c_1, c_2, c_3, c_4 is performed on a single triaxial compression test by using the initial tangential stiffness (or Young's modulus) E_i, the initial Poisson's ratio μ_i, the friction angle ϕ and the dilatancy angle ψ. (Wu and Bauer, 1994 [2] [22]). The calibration procedure of these four parameters is briefly recapitulated.

Figure 2.1 shows a typical triaxial compression test on sand. The test starts from point A and reaches failure at point B. The values of E_i, β_A, β_B, $(\sigma_1 - \sigma_2)_{max}$ (see Figure 2.1) are taken from the test results and used in the calibration.

The two angles β_A and β_B can be expressed by volumetric strain rate $\dot{\epsilon}_v$ and axial strain rate $\dot{\epsilon}_1$ at point A and B,

$$\beta_A = \arctan\left(\frac{\dot{\boldsymbol{\epsilon}}_v}{\dot{\boldsymbol{\epsilon}}_1}\right)_A = \arctan\left(\frac{\dot{\boldsymbol{\epsilon}}_1 + 2\dot{\boldsymbol{\epsilon}}_2}{\dot{\boldsymbol{\epsilon}}_1}\right)_A = \arctan\left(1 + 2\frac{\dot{\boldsymbol{\epsilon}}_2}{\dot{\boldsymbol{\epsilon}}_1}\right)_A \tag{2.11}$$

$$\beta_B = \arctan\left(\frac{\dot{\boldsymbol{\epsilon}}_v}{\dot{\boldsymbol{\epsilon}}_1}\right)_B = \arctan\left(\frac{\dot{\boldsymbol{\epsilon}}_1 + 2\dot{\boldsymbol{\epsilon}}_2}{\dot{\boldsymbol{\epsilon}}_1}\right)_B = \arctan\left(1 + 2\frac{\dot{\boldsymbol{\epsilon}}_2}{\dot{\boldsymbol{\epsilon}}_1}\right)_B \tag{2.12}$$

Because the hypoplastic constitutive model is rate-independent, we can set $\dot{\boldsymbol{\epsilon}}_1 = 1$ to obtain

$$\dot{\boldsymbol{\epsilon}}_2 = \dot{\boldsymbol{\epsilon}}_3 = \frac{1}{2}(1 - \tan\beta) \tag{2.13}$$

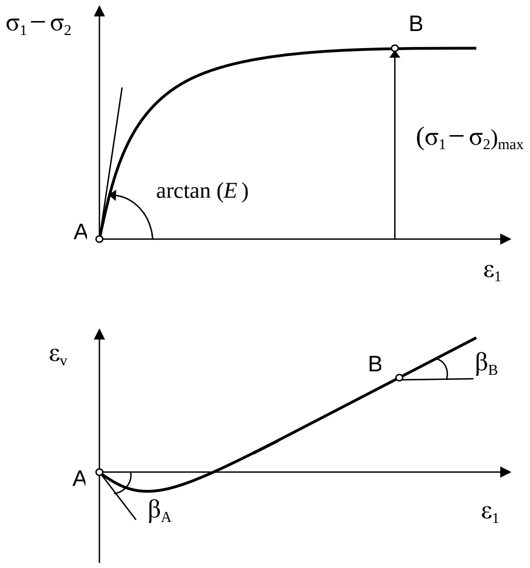

Figure 2.1: Typical triaxial compression test

So the strain rates at point A and B can be shown to be

$$\dot{\boldsymbol{\epsilon}}_A = \begin{pmatrix} -1 & 0 & 0 \\ 0 & \frac{1}{2}(1-\tan\beta_A) & 0 \\ 0 & 0 & \frac{1}{2}(1-\tan\beta_A) \end{pmatrix} \tag{2.14}$$

$$\dot{\boldsymbol{\epsilon}}_B = \begin{pmatrix} -1 & 0 & 0 \\ 0 & \frac{1}{2}(1-\tan\beta_B) & 0 \\ 0 & 0 & \frac{1}{2}(1-\tan\beta_B) \end{pmatrix} \tag{2.15}$$

We consider a triaxial test under constant confining pressure σ_c. The stress tensors at point A and B can be readily written out

$$\sigma_A = \begin{pmatrix} \sigma_{11A} & 0 & 0 \\ 0 & \sigma_{22A} & 0 \\ 0 & 0 & \sigma_{33A} \end{pmatrix} = \begin{pmatrix} \sigma_c & 0 & 0 \\ 0 & \sigma_c & 0 \\ 0 & 0 & \sigma_c \end{pmatrix} \tag{2.16}$$

$$\sigma_B = \begin{pmatrix} \sigma_{11B} & 0 & 0 \\ 0 & \sigma_{22B} & 0 \\ 0 & 0 & \sigma_{33B} \end{pmatrix} = \begin{pmatrix} \sigma_{11B} & 0 & 0 \\ 0 & \sigma_c & 0 \\ 0 & 0 & \sigma_c \end{pmatrix} \tag{2.17}$$

The stress σ_{11B} can be expressed by friction angle and confining pressure as follows

$$\sigma_{11B} = \sigma_c \left(\frac{1 + \sin\phi}{1 - \sin\phi} \right) \tag{2.18}$$

And the stress rate $\dot{\sigma}$ at point A and B are

$$\dot{\sigma}_A = \begin{pmatrix} -E_i & 0 & 0 \\ 0 & 0 & 0 \\ 0 & 0 & 0 \end{pmatrix} \qquad \dot{\sigma}_B = \begin{pmatrix} 0 & 0 & 0 \\ 0 & 0 & 0 \\ 0 & 0 & 0 \end{pmatrix} \tag{2.19}$$

Finally, the parameters c_1, c_2, c_3, c_4 can be determined by solving the following equation system

$$\begin{pmatrix} \mathrm{tr}(\boldsymbol{\sigma}_A)\dot{\epsilon}_{11A} & \frac{\mathrm{tr}(\boldsymbol{\sigma}_A\dot{\boldsymbol{\epsilon}}_A)}{\mathrm{tr}(\boldsymbol{\sigma}_A)}\sigma_{11A} & \frac{\sqrt{\mathrm{tr}(\dot{\boldsymbol{\epsilon}}_A^2)}}{\mathrm{tr}(\boldsymbol{\sigma}_A)}\sigma_{11A}^2 & \frac{\sqrt{\mathrm{tr}(\dot{\boldsymbol{\epsilon}}_A^2)}}{\mathrm{tr}(\boldsymbol{\sigma}_A)}(\sigma_{11A}^*)^2 \\ \mathrm{tr}(\boldsymbol{\sigma}_A)\dot{\epsilon}_{33A} & \frac{\mathrm{tr}(\boldsymbol{\sigma}_A\dot{\boldsymbol{\epsilon}}_A)}{\mathrm{tr}(\boldsymbol{\sigma}_A)}\sigma_{33A} & \frac{\sqrt{\mathrm{tr}(\dot{\boldsymbol{\epsilon}}_A^2)}}{\mathrm{tr}(\boldsymbol{\sigma}_A)}\sigma_{33A}^2 & \frac{\sqrt{\mathrm{tr}(\dot{\boldsymbol{\epsilon}}_A^2)}}{\mathrm{tr}(\boldsymbol{\sigma}_A)}(\sigma_{33A}^*)^2 \\ \mathrm{tr}(\boldsymbol{\sigma}_A)\dot{\epsilon}_{33A} & \frac{\mathrm{tr}(\boldsymbol{\sigma}_B\dot{\boldsymbol{\epsilon}}_B)}{\mathrm{tr}(\boldsymbol{\sigma}_B)}\sigma_{11B} & \frac{\sqrt{\mathrm{tr}(\dot{\boldsymbol{\epsilon}}_B^2)}}{\mathrm{tr}(\boldsymbol{\sigma}_B)}\sigma_{11B}^2 & \frac{\sqrt{\mathrm{tr}(\dot{\boldsymbol{\epsilon}}_B^2)}}{\mathrm{tr}(\boldsymbol{\sigma}_B)}(\sigma_{11B}^*)^2 \\ \mathrm{tr}(\boldsymbol{\sigma}_B)\dot{\epsilon}_{11B} & \frac{\mathrm{tr}(\boldsymbol{\sigma}_B\dot{\boldsymbol{\epsilon}}_B)}{\mathrm{tr}(\boldsymbol{\sigma}_B)}\sigma_{33B} & \frac{\sqrt{\mathrm{tr}(\dot{\boldsymbol{\epsilon}}_B^2)}}{\mathrm{tr}(\boldsymbol{\sigma}_B)}\sigma_{33B}^2 & \frac{\sqrt{\mathrm{tr}(\dot{\boldsymbol{\epsilon}}_B^2)}}{\mathrm{tr}(\boldsymbol{\sigma}_B)}(\sigma_{33B}^*)^2 \end{pmatrix} \begin{pmatrix} c_1 \\ c_2 \\ c_3 \\ c_4 \end{pmatrix} = \begin{pmatrix} -E_i \\ 0 \\ 0 \\ 0 \end{pmatrix} \tag{2.20}$$

The following relationship is useful to relate the angle β_A with the initial Poisson ratio μ_i

$$\tan\beta_A = (1 + 2\mu_i) \tag{2.21}$$

and β_B is the dilatancy angle ψ. Hence we relate the four parameters c$_1$, c$_2$, c$_3$, and c$_4$ to the parameters initial tangential stiffness E_i, the inital Poisson's ratio μ_i, the friction angle ϕ and the dilatancy angle ψ. Equation (2.20) can be easily solved by using the symbolic computational program *Mathematica*.

2.3.3 Implementation of hypoplastic model by Wu in FLAC3D

Equation (2.10) can be implemented in the numerical code FLAC3D, which is widely used in geotechnical engineering. FLAC3D is a finite difference program, which provides user-friendly interfaces to implement user-defined models. For numerical implementation in FLAC3D, the constitutive equation must be written in incremental form. Equation (2.10) can be rewritten in the following incremental form by considering time increment Δt

$$\Delta\boldsymbol{\sigma} = c_1(\mathrm{tr}\boldsymbol{\sigma})\Delta\boldsymbol{\epsilon} + c_2\frac{\mathrm{tr}(\boldsymbol{\sigma}\Delta\boldsymbol{\epsilon})}{\mathrm{tr}\boldsymbol{\sigma}} + (c_3\frac{\boldsymbol{\sigma}^2}{\mathrm{tr}\boldsymbol{\sigma}} + c_4\frac{\boldsymbol{\sigma}^{*2}}{\mathrm{tr}\boldsymbol{\sigma}})\|\Delta\boldsymbol{\epsilon}\| \tag{2.22}$$

The implementation code of the hypoplastic model by Wu can be found in the thesis of Dr. Pornpot Tanseng [16].

2.4 Implementation of an updated hypoplastic model

2.4.1 An updated hypoplastic constitutive equation

Previous studies show that the parameters calibrated for triaxial compression test do not necessarily lead to critical states for other stress paths, e.g. triaxial extension. It was found out that critical state is reached for all paths if the two nonlinear terms are merged into one term by letting (Bauer, 1996 [2])

$$\mathrm{c}_3 = -\mathrm{c}_4 \tag{2.23}$$

As a consequence, the number of parameters in equation (2.10) reduces from four to three.

$$\overset{\circ}{\boldsymbol{\sigma}} = \mathrm{c}_1(\mathrm{tr}\boldsymbol{\sigma})\dot{\boldsymbol{\epsilon}} + \mathrm{c}_2\frac{\mathrm{tr}(\boldsymbol{\sigma}\dot{\boldsymbol{\epsilon}})}{\mathrm{tr}\boldsymbol{\sigma}}\boldsymbol{\sigma} + \mathrm{c}_3(\boldsymbol{\sigma} + \boldsymbol{\sigma}^*)\|\dot{\boldsymbol{\epsilon}}\| \tag{2.24}$$

This severely restricts the adaptability of the model. For instance, the initial Poisson ratio cannot be varied. To resolve this problem, a new term $(\mathrm{tr}\dot{\boldsymbol{\epsilon}})\boldsymbol{\sigma}$ is added to the above equation so that the number of parameters regains four:

$$\overset{\circ}{\boldsymbol{\sigma}} = \mathrm{c}_1(\mathrm{tr}\boldsymbol{\sigma})\dot{\boldsymbol{\epsilon}} + \mathrm{c}_2(\mathrm{tr}\dot{\boldsymbol{\epsilon}})\boldsymbol{\sigma} + \mathrm{c}_3\frac{\mathrm{tr}(\boldsymbol{\sigma}\dot{\boldsymbol{\epsilon}})}{\mathrm{tr}\boldsymbol{\sigma}}\boldsymbol{\sigma} + \mathrm{c}_4(\boldsymbol{\sigma} + \boldsymbol{\sigma}^*)\|\dot{\boldsymbol{\epsilon}}\| \tag{2.25}$$

Note that the same notations for the four parameters are retained in the above equation. Obviously this new term vanishes in critical state with $\mathrm{tr}\dot{\boldsymbol{\epsilon}} = 0$.

2.4.2 Failure surface and flow rule

By the definition of failure, the stress rate at failure vanishes, that is $\overset{\circ}{\boldsymbol{\sigma}} = \mathbf{0}$. Based on this, the failure surface can be derived from constitutive equation (2.25). For simplicity, we may set $\mathrm{c}_1 = 1$. Equation (2.25) can be separated into a spherical part and a deviatoric part. Let us first consider the spherical part, which can be obtained by taking the trace of both sides of equation (2.25)

$$\mathrm{tr}\mathring{\boldsymbol{\sigma}} = (\mathrm{tr}\boldsymbol{\sigma})(\mathrm{tr}\dot{\boldsymbol{\epsilon}}) + \mathrm{c}_2(\mathrm{tr}\dot{\boldsymbol{\epsilon}})(\mathrm{tr}\boldsymbol{\sigma}) + \mathrm{c}_3\frac{\mathrm{tr}(\boldsymbol{\sigma}\dot{\boldsymbol{\epsilon}})}{\mathrm{tr}\boldsymbol{\sigma}}(\mathrm{tr}\boldsymbol{\sigma}) + \mathrm{c}_4(\mathrm{tr}\boldsymbol{\sigma} + \mathrm{tr}\boldsymbol{\sigma}^*)\|\dot{\boldsymbol{\epsilon}}\| \tag{2.26}$$

Note that $\mathrm{tr}\mathring{\boldsymbol{\sigma}} = 0$ and $\mathrm{tr}\dot{\boldsymbol{\epsilon}} = 0$ in a critical state. We make use of the relation $\boldsymbol{\sigma}^* = \boldsymbol{\sigma} - \frac{1}{3}(\mathrm{tr}\boldsymbol{\sigma})\mathbf{1}$ and $\mathrm{tr}(\boldsymbol{\sigma}^*\dot{\boldsymbol{\epsilon}}^*) = \|\boldsymbol{\sigma}^*\|\|\dot{\boldsymbol{\epsilon}}^*\|\cos\theta$, with θ being the angle between $\boldsymbol{\sigma}^*$ and $\dot{\boldsymbol{\epsilon}}^*$ and $\dot{\boldsymbol{\epsilon}}^*$ is the deviatoric strain rate. The following equation can be obtained by letting $\mathrm{tr}\mathring{\boldsymbol{\sigma}} = 0$

$$\mathrm{c}_3\|\boldsymbol{\sigma}^*\|\|\dot{\boldsymbol{\epsilon}}^*\|\cos\theta + \mathrm{c}_4\mathrm{tr}\boldsymbol{\sigma}\|\dot{\boldsymbol{\epsilon}}\| = 0 \tag{2.27}$$

Let r_c denotes the stress ratio $\|\boldsymbol{\sigma}^*\|/\mathrm{tr}\boldsymbol{\sigma}$ in a critical state. From the above equation we can get

$$\mathrm{c}_3 r_c\cos\theta + \mathrm{c}_4 = 0 \tag{2.28}$$

The term $\cos\theta$ represents the flow direction with reference to the stress in a critical state. As will be shown thereafter, we have $\cos\theta = 1$. In this case, the follwoing relationship between c_3 and c_4 is obtained from the equation (2.28)

$$-\frac{\mathrm{c}_4}{\mathrm{c}_3} = r_c \tag{2.29}$$

It is clear that equation (2.29) represents the failure criterion of Drucker-Prager ([21], [19], [27]). Now, let us turn our attention to the deviatoric part of the consitutive equation (2.25)

$$\mathring{\boldsymbol{\sigma}}^* = (\mathrm{tr}\boldsymbol{\sigma})\dot{\boldsymbol{\epsilon}}^* + \mathrm{c}_2(\mathrm{tr}\dot{\boldsymbol{\epsilon}})\boldsymbol{\sigma}^* + \mathrm{c}_3\frac{\|\boldsymbol{\sigma}^*\|\|\dot{\boldsymbol{\epsilon}}^*\|}{\mathrm{tr}\boldsymbol{\sigma}}\cos\theta\boldsymbol{\sigma}^* + 2\mathrm{c}_4\boldsymbol{\sigma}^*\|\dot{\boldsymbol{\epsilon}}\| = 0 \tag{2.30}$$

We make use of $\mathrm{tr}\dot{\boldsymbol{\epsilon}} = 0$ and $\mathrm{tr}(\boldsymbol{\sigma}\dot{\boldsymbol{\epsilon}}) = \mathrm{tr}(\boldsymbol{\sigma}^*\dot{\boldsymbol{\epsilon}}^*) = \|\boldsymbol{\sigma}^*\|\|\dot{\boldsymbol{\epsilon}}^*\|\cos\theta$ and $\|\dot{\boldsymbol{\epsilon}}\| = \|\dot{\boldsymbol{\epsilon}}^*\|$ to get

$$\frac{\dot{\boldsymbol{\epsilon}}^*}{\|\dot{\boldsymbol{\epsilon}}^*\|} = -(\mathrm{c}_3 r_c\cos\theta + 2\mathrm{c}_4)\frac{\boldsymbol{\sigma}^*}{\mathrm{tr}\boldsymbol{\sigma}} \tag{2.31}$$

The above equation indicates that the stress tensor and the strain rate tensor are coaxial in a critical state. This can be also expected for the failure surface of Durcker-Prager ([21], [19], [27]). Note that $(\dot{\boldsymbol{\epsilon}}^*/\|\dot{\boldsymbol{\epsilon}}^*\|) : (\dot{\boldsymbol{\epsilon}}^*/\|\dot{\boldsymbol{\epsilon}}^*\|) = 1$ we have

$$\mathrm{c}_3{r_c}^2\cos\theta + 2\mathrm{c}_4 r_c - 1 = 0 \tag{2.32}$$

The above equation is quardratic in r_c. Combining equation (2.29) and equaion (2.32), we can solve for c$_3$ to get

$$\mathrm{c}_3 = -\frac{1}{{r_c}^2} \tag{2.33}$$

The paramters c$_3$ can be set into equation (2.29) to give c$_4$

$$\mathrm{c}_4 = \frac{1}{r_c} \tag{2.34}$$

Then equation (2.25) can be rewritten as follows after the parameters are specified by equations (2.33) and (2.34)

$$\|\boldsymbol{\sigma}^*\| = r_c(\mathrm{tr}\boldsymbol{\sigma}) \tag{2.35}$$

It is noteworthy that equation (2.35) is similar to the failure formula proposed by Bardet (1990) [1]. This formula has the advantage that it encompassed two widely used failure criteria Matsuoka-Nakai (1974) [13] and Lade-Duncan (1975) [12].

2.4.3 Calibration procedure of parameters

As menstioned in Section 2.3.2, the four parameters c_1, c_2, c_3, c_4 can be calibrated using the initial tangential stiffness E_i, the initial Poisson's ratio μ_i, the friction angle ϕ and the dilatancy angle ψ based on a single triaxial compression test. For the updated hypopalstic model, the four parameters can be calculated by solving the following equation system.

$$\begin{pmatrix} \mathrm{tr}(\boldsymbol{\sigma}_A)\dot{\epsilon}_{11A} & \mathrm{tr}(\dot{\boldsymbol{\epsilon}}_A)\sigma_{11A} & \dfrac{\mathrm{tr}(\boldsymbol{\sigma}_A\dot{\boldsymbol{\epsilon}}_A)}{\mathrm{tr}(\boldsymbol{\sigma}_A)}\sigma_{11A} & s_{11A} \\ \mathrm{tr}(\boldsymbol{\sigma}_A)\dot{\epsilon}_{33A} & \mathrm{tr}(\dot{\boldsymbol{\epsilon}}_A)\sigma_{33A} & \dfrac{\mathrm{tr}(\boldsymbol{\sigma}_A\dot{\boldsymbol{\epsilon}}_A)}{\mathrm{tr}(\boldsymbol{\sigma}_A)}\sigma_{33A} & s_{33A} \\ \mathrm{tr}(\boldsymbol{\sigma}_B)\dot{\epsilon}_{11B} & \mathrm{tr}(\dot{\boldsymbol{\epsilon}}_B)\sigma_{11B} & \dfrac{\mathrm{tr}(\boldsymbol{\sigma}_B\dot{\boldsymbol{\epsilon}}_B)}{\mathrm{tr}(\boldsymbol{\sigma}_B)}\sigma_{11B} & s_{11B} \\ \mathrm{tr}(\boldsymbol{\sigma}_B)\dot{\epsilon}_{33B} & \mathrm{tr}(\dot{\boldsymbol{\epsilon}}_B)\sigma_{33B} & \dfrac{\mathrm{tr}(\boldsymbol{\sigma}_B\dot{\boldsymbol{\epsilon}}_B)}{\mathrm{tr}(\boldsymbol{\sigma}_B)}\sigma_{33B} & s_{33B} \end{pmatrix} \begin{pmatrix} c_1 \\ c_2 \\ c_3 \\ c_4 \end{pmatrix} = \begin{pmatrix} -E_i \\ 0 \\ 0 \\ 0 \end{pmatrix} \tag{2.36}$$

where $s_{11A} = \sigma_{11A} + \sigma^*_{11A}$, $s_{33A} = \sigma_{33A} + \sigma^*_{33A}$, $s_{11B} = \sigma_{11B} + \sigma^*_{11B}$, $s_{33B} = \sigma_{33B} + \sigma^*_{33B}$. The stress tensors $\boldsymbol{\sigma}_{A/B}$ and the strain rate tensors $\dot{\boldsymbol{\epsilon}}_{A/B}$ can be determined from the initial tangential stiffness E_i, the initial Poisson's ratio μ_i, the friction angle ϕ and the dilatancy angle ψ (see equations (2.14), (2.15), (2.16), (2.17), (2.18), (2.21)).

2.4.4 Implementaion of the updated hypoplastic model in FLAC3D

The hypoplastic constitutive equation (2.10) is originally developed for sand. In practice, however, most soils show cohesion to some extent. Therefore, it is important to take cohesion into consideration. For cohesive materials, the constitutive equation (2.25) is extended by replacing the stress tensor $\boldsymbol{\sigma}$ with the following translated stress tensor

$$\boldsymbol{\eta} = \boldsymbol{\sigma} - c\mathbf{1} \tag{2.37}$$

where c is cohesion. Then the hypoplastic constitutive equation (2.25) can be rewritten as follows

$$\overset{\circ}{\boldsymbol{\sigma}} = \mathrm{c}_1(\mathrm{tr}\boldsymbol{\eta})\dot{\boldsymbol{\epsilon}} + \mathrm{c}_2(\mathrm{tr}\dot{\boldsymbol{\epsilon}})\boldsymbol{\eta} + \mathrm{c}_3\frac{\mathrm{tr}(\boldsymbol{\eta}\dot{\boldsymbol{\epsilon}})}{\mathrm{tr}\boldsymbol{\eta}}\boldsymbol{\eta} + \mathrm{c}_4(\boldsymbol{\eta} + \boldsymbol{\eta}^*)\|\dot{\boldsymbol{\epsilon}}\| \tag{2.38}$$

By considering time increment Δt, we can get the following incremental form

$$\Delta\sigma = \mathrm{c}_1(\mathrm{tr}\boldsymbol{\eta})\Delta\boldsymbol{\epsilon} + \mathrm{c}_2(\mathrm{tr}\Delta\boldsymbol{\epsilon})\boldsymbol{\eta} + \mathrm{c}_3\frac{\mathrm{tr}(\boldsymbol{\eta}\Delta\boldsymbol{\epsilon})}{\mathrm{tr}\boldsymbol{\eta}}\boldsymbol{\eta} + \mathrm{c}_4(\boldsymbol{\eta} + \boldsymbol{\eta}^*)\|\Delta\boldsymbol{\epsilon}\| \tag{2.39}$$

When implementing the constitutive model in FLAC3D, the explicit form of equation (2.39) is needed. FLAC3D uses different coordinate notations for model implementation as shown in Figure (2.2). We proceed to write out equation (2.39) explicitly

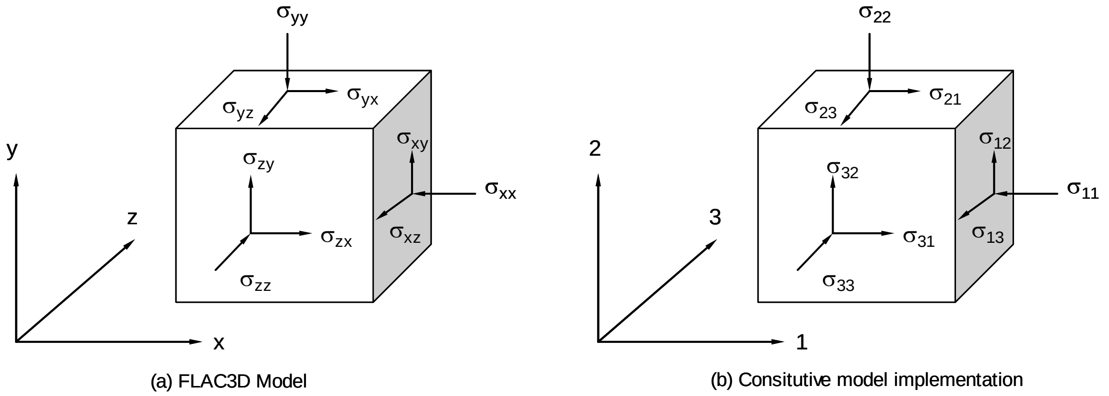

Figure 2.2: Coordinates and stresses notations

$$\begin{aligned}
\Delta\sigma_{11} &= \mathrm{c}_1(\mathrm{tr}\boldsymbol{\eta})\Delta\epsilon_{11} + \mathrm{c}_3\frac{\mathrm{tr}(\boldsymbol{\eta}\Delta\boldsymbol{\epsilon})}{\mathrm{tr}\boldsymbol{\eta}}\eta_{11} + \mathrm{c}_4(\eta_{11} + \eta^*_{11})\|\Delta\boldsymbol{\eta}\| \\
\Delta\sigma_{22} &= \mathrm{c}_1(\mathrm{tr}\boldsymbol{\eta})\Delta\epsilon_{22} + \mathrm{c}_3\frac{\mathrm{tr}(\boldsymbol{\eta}\Delta\boldsymbol{\epsilon})}{\mathrm{tr}\boldsymbol{\eta}}\eta_{22} + \mathrm{c}_4(\eta_{22} + \eta^*_{22})\|\Delta\boldsymbol{\eta}\| \\
\Delta\sigma_{33} &= \mathrm{c}_1(\mathrm{tr}\boldsymbol{\eta})\Delta\epsilon_{33} + \mathrm{c}_3\frac{\mathrm{tr}(\boldsymbol{\eta}\Delta\boldsymbol{\epsilon})}{\mathrm{tr}\boldsymbol{\eta}}\eta_{33} + \mathrm{c}_4(\eta_{33} + \eta^*_{33})\|\Delta\boldsymbol{\eta}\| \\
\Delta\sigma_{12} &= \mathrm{c}_1(\mathrm{tr}\boldsymbol{\eta})\Delta\epsilon_{12} + \mathrm{c}_3\frac{\mathrm{tr}(\boldsymbol{\eta}\Delta\boldsymbol{\epsilon})}{\mathrm{tr}\boldsymbol{\eta}}\eta_{12} + \mathrm{c}_4(\eta_{12} + \eta^*_{12})\|\Delta\boldsymbol{\eta}\| \\
\Delta\sigma_{13} &= \mathrm{c}_1(\mathrm{tr}\boldsymbol{\eta})\Delta\epsilon_{13} + \mathrm{c}_3\frac{\mathrm{tr}(\boldsymbol{\eta}\Delta\boldsymbol{\epsilon})}{\mathrm{tr}\boldsymbol{\eta}}\eta_{13} + \mathrm{c}_4(\eta_{13} + \eta^*_{13})\|\Delta\boldsymbol{\eta}\| \\
\Delta\sigma_{23} &= \mathrm{c}_1(\mathrm{tr}\boldsymbol{\eta})\Delta\epsilon_{23} + \mathrm{c}_3\frac{\mathrm{tr}(\boldsymbol{\eta}\Delta\boldsymbol{\epsilon})}{\mathrm{tr}\boldsymbol{\eta}}\eta_{23} + \mathrm{c}_4(\eta_{23} + \eta^*_{23})\|\Delta\boldsymbol{\eta}\|
\end{aligned} \tag{2.40}$$

In FLAC3D, the user-defined constitutive model is written in C++ and compiled as DLL (dynamic link library) ([6]). The model can be then loaded into FLAC3D for calculations. The user-defined models written in this way are as efficient as the built-in models. Afterawards, the code need be verified against some benchmark problems.

Chapter 3

Numerical Implementation and Verificiation

In this chapter a brief description of FLAC3D is given. A user-firendly interface is provided in FLAC3D to implement user-defined constitutive model. The numerical implementation of the updated hypoplastic constitutive equations in FLAC3D is presented. The code is verified with some laboratory experiments.

3.1 Backfround of FLAC3D

3.1.1 Introduction

FLAC3D (Fast Lagrangian Analysis of Continua 3 Dimension) is a three-dimensional explicit finite difference program for engineering mechanics computation. In the explicit finite difference method, every derivate in the governing equations is converted into algebraic expression written in terms of the undefined field variables (e.g. stress or displacement) at discrete points in space.

FLAC uses an explicit time integration method to solve the algebraic equations generated at each step. By using the full dynamic equations of motion, FLAC ensures that the numerical scheme is stable even if the situation being modeled is unstable (The principle will not be repeated in this thesis and readers can find the details in FLAC3D manual books [6]). FLAC3D simulates the behavior of three-dimensional structure built of soil, rock or other materials that undergo plastic flow when their yield limits are reached. The calculation procedure of FLAC3D is shown in Figure 3.1. First, new strain rates are derived from nodal velocities, then constitutive equations are used to calculate new stresses from the strain rates and stresses at the previous time, and the equations of motion are invoked to derive new nodal velocities and displacements from new stresses and forces. The sequence is repeated at every timestep, and the maximum out-of-balance force in the model is monitored. This force will either approach zero, indicating that the system is reaching an equilibrium state, or it will approach a constant, nonzero value, indicating that a portion (or all) of the system is at steady-state (plastic) flow of material. One of the advantages of this procedure is that no iteration process is required in computing stress increments from strain increments in an element, even when the constitutive law is highly nonlinear.

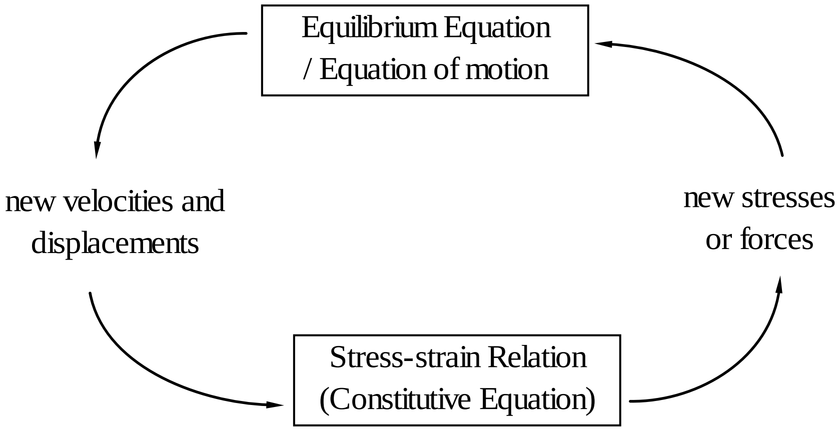

Figure 3.1: Explicit calculation procedures in FLAC3D

3.1.2 Mathematical model description

IFLAC3D is an explicit finit difference program to study numerically the mechanical behaviour of continuous three-dimensional medium as it reaches equilibrium or steady plastic folw. In FLAC3D, the medium is discretized into constant strain-rate elements of tetrahedral shape as shown in Figure 3.2 .

The mechanics of the medium are derived from general principles (definition of strain, laws of motion), and the use of constitutive equations defining the idealized material. The materials can yield and flow and the grid can deform (in large-strain mode) and move with the material that is represented. The resulting mathematical expression is a set of partial differential equations, relating mechanical (stress) and kinematical (strain rate, velocity) variables, which are to be solved for particular geometries and properties, given specific boundary and initial conditions.

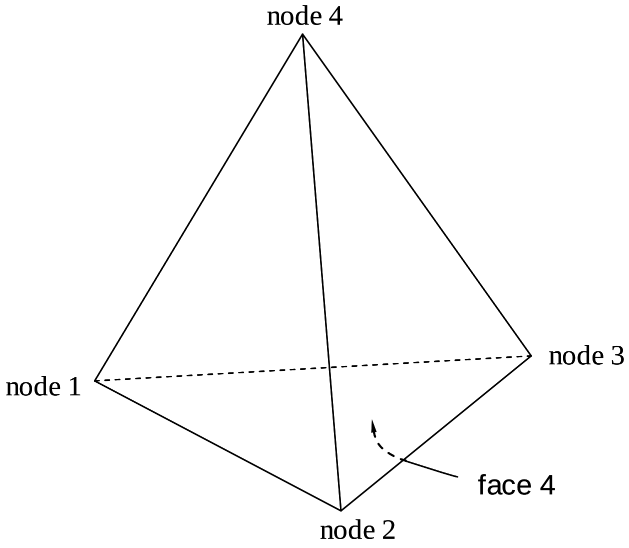

Figure 3.2: Tetrahedron element

Conventions

In Lagrangian formulation adopted in FLAC3D, a point in the medium is characterized by vector components x_i, u_i, v_i and dv_i/dt, $i = 1, 2, 3$ of position, displacement, velocity and acceleration respectively. By definition, tension and extension are positive.

The state of stress at a given point of the medium is characterized by the symmetric stress tensor σ_{ij}. The traction vector $[t]$ on an infinitesimal area with unit normal $[n]$ is given by

$$t_i = \sigma_{ij} n_{ij} \tag{3.1}$$

In an infinitesimal time dt, the medium experiences an infinitesimal strain determined by the translations $v_i dt$, and the corresponding components of the strain-rate tensor may be written as

$$\xi_{ij} = \frac{1}{2}(v_{i,j} + v_{j,i}) \tag{3.2}$$

where partial derivatives are taken with respect to components of the current position vector $[x]$.

In addtion to the strain-rate tensor ξ_{ij}, a volume element may experience an instantaneous rigid-body displacement determined by the translation velocity $[v]$ and a rotation with angular velocity Ω_i,

$$\Omega_i = -\frac{1}{2} e_{ijk} \omega_{jk} \tag{3.3}$$

where e_{ijk} is the permutation symbol and $[\omega]$ is the rate of rotation tensor whose components are defined as

$$\omega_{ij} = \frac{1}{2}(v_{i,j} - v_{j,i}) \tag{3.4}$$

Equations of Motion and Equilibrium

Application of the continuum form of the momentum principle yields Cauchy's equations of motion:

$$\sigma_{ij,k} + \rho b_i = \rho \frac{dv_i}{dt} \tag{3.5}$$

where is ρ the mass per unit volume of the medium, $[b]$ is the body force per unit mass, and $d\,[v]\,/dt$ is the material derivative of the velocity. Note that, in the case of static equilibrium of the medium, the acceleration $d\,[v]\,/dt$ is zero, so the equation (3.5) could be rewritten as follows

$$\sigma_{ij,k} + \rho b_i = 0 \tag{3.6}$$

Boundary and Initial Conditions

The boundary conditions consist of imposed boundary tractions and displacements. In addition, body forces may be present, and also, the initial stress state of body needs to be specified.

Constitutive Equations

There are fifteen unknowns in the motion equations (3.5) and the definition of strain-rate (Equation 3.2). These unknowns are six components of the stress rate, six components of strain rate, and three components of the velocity vector. There are six additional relations provided by the constitutive equations. The constitutive equations define the nature of the particular material under consideration. They are given in the following form

$$[\mathring{\boldsymbol{\sigma}}]_{ij} = \mathbf{H}_{ij}(\sigma_{ij}, \xi_{ij}, \kappa) \tag{3.7}$$

where $[\mathring{\boldsymbol{\sigma}}]_{ij}$ is the co-rotational stress-rate tensor, $[\mathbf{H}]$ is a given function, and κ is a parameter that takes into account the history of loading. Generally, non-linear constitutive laws are written in incremental or rate form because the relationship between stress and strain is not unique. The co-rational stress rate $[\mathring{\boldsymbol{\sigma}}]$ is equal to the material derivative of the stress as it would appear to an observer in a frame of reference attached to the material point and rotating with it at an angular velocity equal to the instantaneous value of the angular velocity $[\Omega]$ of the material. The stress-rate tensor is defined as

$$[\mathring{\boldsymbol{\sigma}}]_{ij} = \frac{d\sigma_{ij}}{dt} - \omega_{ik}\sigma_{kj} + \sigma_{ik}\omega_{kj} \tag{3.8}$$

where $d\,[\boldsymbol{\sigma}]\,/dt$ is the material time derivative of $[\boldsymbol{\sigma}]$, and $[\omega]$ is the rate of rotation tensor.

3.1.3 Numerical implementation issues

Body discretization

In FLAC3D, the discretization of the body into zones is performed by the user. Each zone is discretized automatically by the code into sets of tetrahedral. The user can decide to carry out the calculation using one overlay or a combination of two overlays. The use of two overlays is recommended in regions where high gradients of stressed and deformations are expected. By default, two overlays are presented for all zones in a model. The details about body discretization can be found in FLAC3D manual books ([6]).

Initial and boundary conditions

The boundary conditions of the problem consist of surface tractions, concentrated loads and displacements. In addition, body forces may be given and initial stress conditions imposed. For implementation in the code, all stresses and nodal velocities are initially set to zero; then, initial stresses are specified. Concentrated loads are specified at a given surface nodes, and imposed boundary displacements are prescribed in terms of nodal velocities. Body forces and surface tractions are transformed internally into a set of statically equivalent nodal forces. This constitutes the initial state of the numerical scheme.

Main calculation steps

FLAC3D uses an explicit 'time-marching' finite difference solution scheme; for every timestep, the calculation sequence can be summarized as follows.

1. New strain rates are derived from nodal velocities.
2. Constitutive equations are used to calculate new stresses from the strain rates and stresses at the previous time.

3. The equations of motion are invoked to derive new nodal velocities and displacements from stresses and forces.

The sequence is repeated at every timestep, and the maximum out-of-balance force in the model is monitored. This force will either approach to zero, indicating that the system is reaching an equilibrium state, or it will approach a constant, nonzero value, indicating that a portion (or all) of the system is at steady-state flow of material. The calculation may be interrupted at any point in order to analyze the solution.

3.1.4 Constitutive Models

There are twelve basic constitutive models provided in FLAC3D Version 3.0, arranged into null, elastic and plastic model group.

Null model group includes null model. This null model is used to represent materials that are to be removed or excavated. Elastic model group includes elastic isotropic model, elastic orthotropic model, and elastic transversely isotropic model. Plastic model group includes Drucker-Prager model, Mohr-Coulomb model, ubiquitous-joint model, strain-hardening/softening model, bilinear strain-hardening / softening ubiquitous-joint model, double-yield model, modified Cam-clay model and Hoek-Brown model.

Besides these twelve constitutive models, users are allowed to define their own constitutive models for incorporation into FLAC3D. The main function of user-defined models is to return new stresses for stain increments. The models must also provide other information, such as names, and perform operations such as writing and reading save files. In FLAC3D there is no FISH (a programming language embedded within FLAC3D that enables the user to define new variables and functions) framework for adding constitutive models (unlike in FLAC), the User-defined constitutive models must be written in C++, and compiled as DLL (dynamic link library) files that can be loaded whenever needed. C++ DLL models run at the same speed as built-in models in FLAC3D. The methodology of writing a constitutive model is described in FLAC3D manual. Here the methodology of writting a constitutive model in C++ for operation in FLAC3D is introduced briefly as follows:

1. *Base Class for Constitutive Models*

   In the C++ language, the emphasis is on an object oriented approach to program structure, using classes to present objects. The data associated with an object are encapsulated by the object and are invisible outside the object. In the source code of user-defined models, a base class called **ConstitutiveModel** is used to provide a framework for actual constitutive models. This base class declares a number of "pure virtual" member functions which must be replaced by actual functions from derived constitutive-model class. Some members of **ConstitutiveModel** as utility functions are self-evident. Other functions are used by FLAC3D to manipulate and interrogate constitutive models. All these functions are already defined in the source code files which are provided by FLAC3D; there is no need for a user-written model to use or redefine these. The details of operation performed by these functions can be found in FLAC3D manual. Besides these functions, the model class definition should also contain a constructor that must invoke the base constructor. If the base constructor is called with **bRegister**, set **true**, then the derived model is ***registered*** with FLAC3D. A type number unique to the model must also be passed; this enables the correct model to be reinstalled in each zone when a problem is restored from a save file, which is a binary file containing the values of all state variables and user-defined conditions. A save file can be restored and the analysis continued at a subsequent time.

2. *Registration of Models*

   Each user-written constitutive model contains its own name and the name of its properties and state indicators. FLAC3D can recognize this information by calling the appropriate member function. FLAC3D is made aware of a user-written constitutive model by a *constructor call* that is invoked by a static global instance of a model object. The object is constructed either when FLAC3D is loaded (for the "built-in" models), or when a DLL is loaded (for external models). The **true** value of the argument causes the base constructor to "register" the new model, and add it to the list of models.

3. *Information Passed between Model and FLAC3D during Cycling*

   A user-written model and FLAC3D is linked by the member-function **Run**(), which computes the mechanical response of the model during cycling. A structure, **State**, is used to transfer information to and from the model. The main task of member-function **Run**() is to compute new stresses from strain increments. In a nonlinear model, it is also useful to communicate the internal state of the model, so that the state may be plotted and printed. For example, the supplied models indicate whether they are currently yielding or have yielded in the past. Each sub-zone may set the variable **mState**, which records the state of a model as a series of bits that can be on or off (1 or 0). Each bit can be associated with a message that is displayed on the screen.

4. *State Indicators of Zones*

   A zone in FLAC3D is comprised of tetrahedral sub-zones, and each tetrahedral sub-zone has a member variable that maintains its current state indictor. For user-defined constitutive models, the user can create a named state and assign any particular bit for that state, and subsequently update the tetrahedral state indicator variable. Users just need to make sure that there is no conflict with failure sate constants of the built-in models if they plan to use both of them in an analysis. FLAC3D calls the constitutive model function **Run**() for each tetrahedron that makes up the zone to updated its stress values. Typically, the state indicator is also updated this process by the constitutive model. The user should take care to set or unset appropriately, all previous states updated prior to the current state calculated by the constitutive model.

5. *Implementation*

   In order to create a DLL in Visual C++, it is first necessary to create a workspace. The workspace will contain projects that are essentially a collection of C++ source and header files and their dependencies. The following four head files should be included in the project. They are AXES.H, CONMODEL.H, CONTABLE.H, and STENSOR.H. The "AXES.H" head file specifies a particular axes system. The "CONMODEL.H" head file defines utility structure used to communicate with constitutive model. The "CONTABLE.H" head file defines the TABLE interface for general constitutive models. The "STENSOR.H" head file stores symmetric tensors. These four head files are provided by FLAC3D. There is no need for a user-written model to redefine them. Besides these head files, there are two more files which should also be included. One is the head file of the user-defined model. This head file provides the class specification for the model, which defines some private variables of the model for internal use only. Another is the C++ source file which provides the listings of the member functions for initialization and execution. About creating DLL file from a workspace, user can refer to Microsoft VC++ documentation for detailed information.

> Before user-defined models can be loaded into FLAC3D, the code must first be configured to accept DLL models by giving the **CONFIG cppudm** command. Model DLL files may then be loaded into FLAC3D by giving the command **MODEL load**<filename> while FLAC3D is running.

More details about writing new constitutive models in FLAC3D can be found in FLAC3D manual books ([6]). Once the selected hypoplastic constitutive model is coded and compiled as DLL, it could be built into FLAC3D and loaded. Afterwards, the code need be verified against some bechmark problems. In this chapter, four laboratory tests are simulated, i.e. isptropic compression test, triaxial tests, biaxial test and simple shear test.

3.2 Simulation of isotropic compression test

3.2.1 Problem statement

Isotropic compression test is the simplest test to study the stress-strain behaviours of soil. Figure 3.3 shows the stresses and deformation in an isotropic compression test.

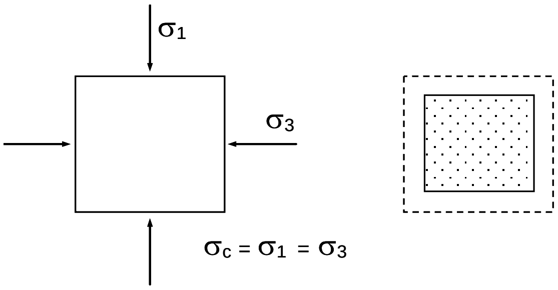

Figure 3.3: Stresses and deformation in a isotropic compression test

The material properties are showed in Table 3.1. The corresponding parameters of hypoplastic model are shown in Table 3.2.

Table 3.1: Material parameters

E [MPa]	μ [-]	ψ [°]	ϕ [°]	c [kPa]
2	0.2	15	30	0

Table 3.2: Corresponding coefficients of hypoplastic model

c_1	c_2	c_3	c_4
-5.56	-81.51	-9.57	-18.01

3.2.2 FLAC3D Model

The specimen is modelled as a cube in FLAC3D (Figure 3.4). Initially, the model is fixed for displacements in x-, y-, z-directions. The compression test is started with an initial stress of 5 Pa and simulated by applying nodal velcotiy. A constant velocity of 5×10^{-5} m/step is applied to the boundary faces located at x = 1, y = 1 and z = 1 of the model in the negative x-, y-, z-direction, for a total of 1000 steps.

An unloading-reloading is simulated too. Loading excursion is simulated by applying a constant velocity of 5×10^{-5} m/step to the boundary faces located at x =1, y = 1 and z =1 of the model in the negative x-, y-, z-direction, after 400 steps, the unloading procedure is started by applying a constant velocity of 5×10^{-6} m/step to the boundary faces located at x = 1, y = 1 and z = 1 of the model in the positive x-, y-, z-direction, after 500 steps, reloading excursion is started by applying a constant velocity of 5×10^{-5} m/step to the boundary faces located at x = 1, y = 1 and z = 1 of the model in the negative x-, y-, z-direction for 800 steps. This loading-unloading excursion is simulated by 3 loops.

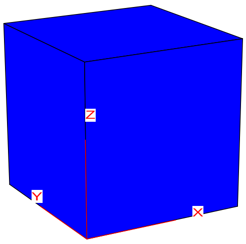

Figure 3.4: FLAC3D model

3.2.3 Numerical results

The numerical results of the isotropic compression test are shwon in Figure 3.5 and Figure 3.6.

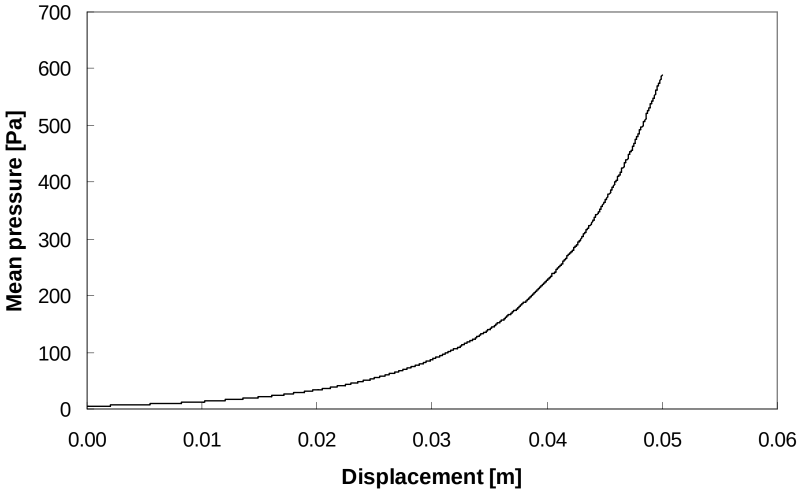

Figure 3.5: Mean pressure vs.displacement

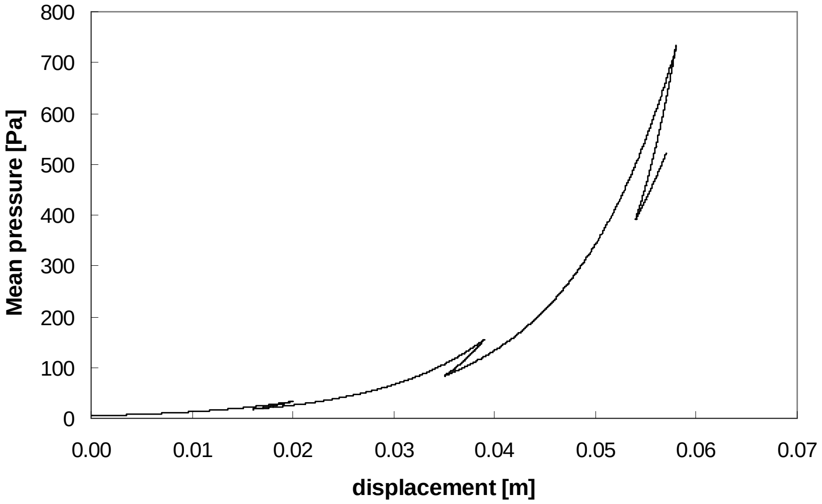

Figure 3.6: Mean pressure vs. displacement under unload-reload excursion

From Figure 3.5, we can see that axial strain gets stiffer as the level of stress increases, which is well known from laboratory tests. The numerical result of isotropic compression test subjected to unload-reload excursion shows one of the advantages of hypoplastic constitutive model that no extra definition for loading and unloading is needed. However, the loops of the pressure-displacement curve during unloading-reloading are not closed. This is due to the fact that the history dependence is represented by the instantaneous stress, which is obviously not enough for complex loading paths involving unloading and reloading.

3.3 Simulation of triaxial test

3.3.1 Problem statement

Triaxial test is the most common test used to determine the stress-strain properties of soil. Here a conventional drained triaxial test is simulated. The material properties are used from Table 3.3. The corresponding hypoplastic parameters are shown in Table 3.4.

Table 3.3: Material parameters used in the triaxial test

E [MPa]	μ [-]	ψ [°]	ϕ [°]	c [kPa]
17	0.2	15	30	0/100

Table 3.4: Corresponding coefficients of hypoplastic model

c_1	c_2	c_3	c_4
-47.22	-692.84	-81.36	-153.05

3.3.2 FLAC3D model

The sepcimen is modelled as one single zone with unit dimensions (Figure 3.4). Initially, the specimen is in an isotropic stress state. The test is carried out with constant confining pressure and simulated by applying the vertical velocity while keeping the lateral stress constant. Besides triaxial compression test, a triaxial extension test and a triaxial test with loading-reloading excursions are simulated.

For the hypoplastic model with cohesion, an unconfined compression test with a cohesion of 100 kPa (Table 3.3) is compared with a triaxial compression test without cohesion under a confining pressure of 100 kPa.

In the simulation of the triaxial compression test, the initial velocity of 0.1×10^{-4} m/step is applied to the boundary face located at z = 1 in the negative z- direction. A total of 10000 steps with a velocity magnitude of 0.1×10^{-4} m/step is used to simulate the loading excursion. This constant compressive velocity is applied to the boundary face located at z = 1 in the negative z-direction.

In the simulation of triaxial extension test, the initial velocity of 0.1×10^{-4} m/step is applied to the boundary face located at z = 1 of the model in the positive z- direction.

A total of 8000 steps with a velocity magnitude of 0.1×10^{-4} m/step is used to simulate the extension. In this case a constant velocity is applied to the boundary face located at z = 1 of model in the positive z-direction.

For the loading-unloading excursion, the loading part is similar with the compression test, after 8000 steps of compression with a constant velocity of 0.1×10^{-4} m/step, a new constant velocity - 0.1×10^{-5} m/step (unloading) is applied to the top of model (z = 1) in the positive z-direction for 2000 steps.

For the hypoplastic model with cohesion, an unconfined compression test with a cohesion of 100 kPa (see Table 3.3) is compared with a triaxial compression test without cohesion under a confining pressure of 100 kPa.

3.3.3 Numerical results

Figure 3.7 and Figure 3.8 show the numerical results of triaxial compression and extension test. Figure 3.9 shows the numerical result of the triaxial test subjected to loading-unloading.

The FLAC3D simulations in Figure 3.7 and Figure 3.8 are well corroborated by numerical simulations of one element as described by Wu and Bauer (1994)[22]. The simulation result in Figure 3.9 shows one of the advantages of hypoplastic constitutive model that loading and unloading are implied by the constitutive equation and there is no need to define them explicitly.

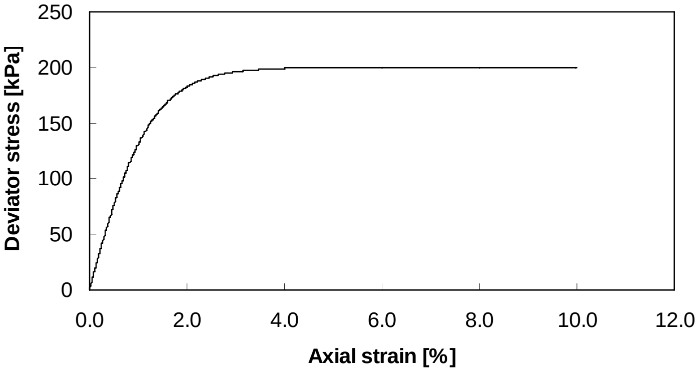

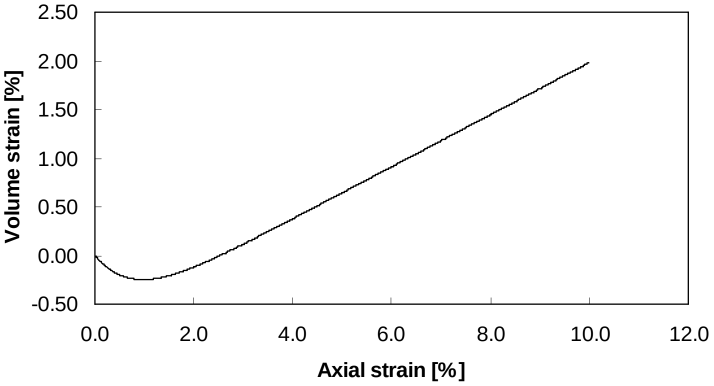

Figure 3.7: Numerical results of triaxial compression test

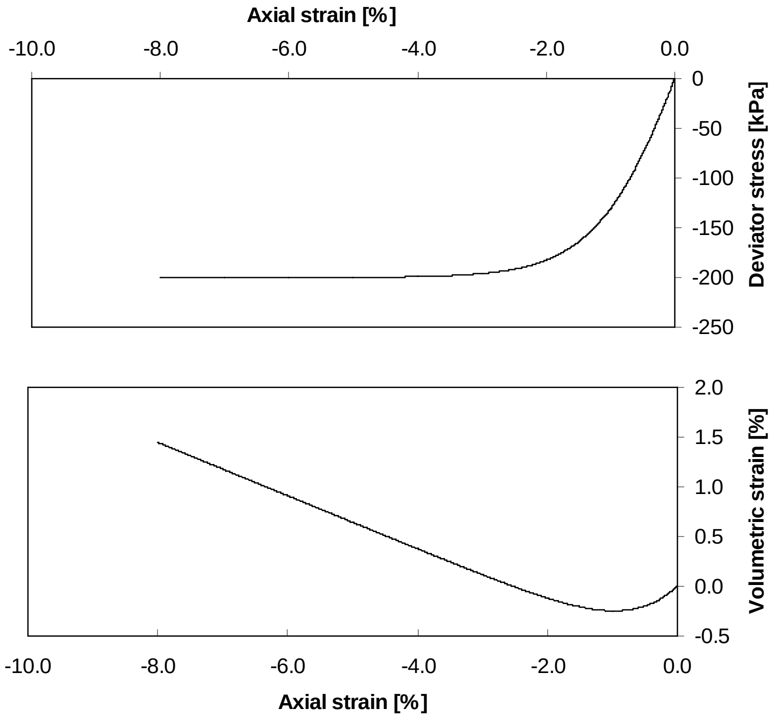

Figure 3.8: Numerical results of triaxial extension test

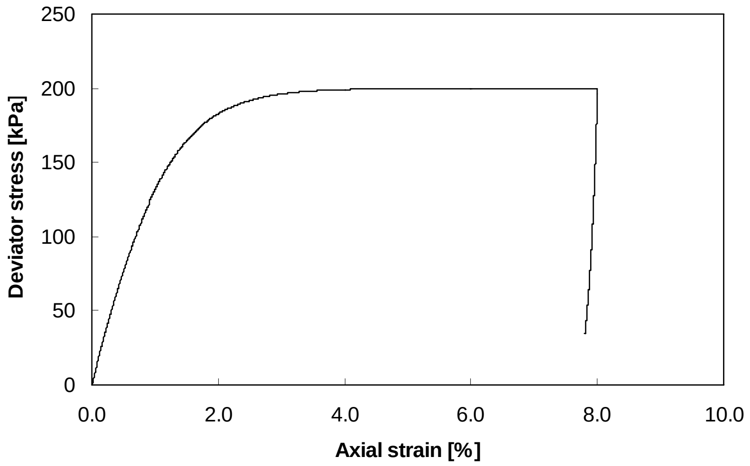

Figure 3.9: Numerical results of triaxial test subjected to unloading excursion

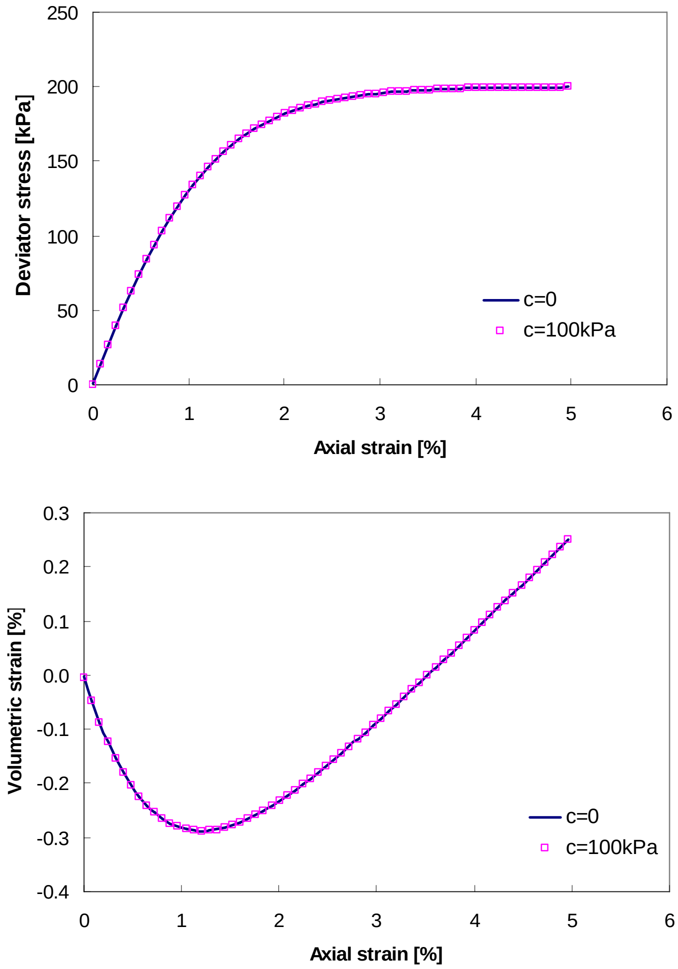

Figure 3.10: Comparison between unconfined compression test and triaxial compression test with a confining pressure of 100 kPa

Figure 3.10 can be appreciated by considering the Mohr-Coulomb failure criterion. The following relationship between cohesion and unconfined compressive strength can be easily shown

$$c = \frac{1 - \sin\phi}{2\sin\phi}\sigma_p \tag{3.9}$$

where σ_p is the unconfined compressive strength. According the above relationship, an unconfined compression test with a given cohesion is equivalent to a triaxial compression test under certain confining pressure without cohesion. After equation (3.9), the unconfined compressive strength for a friction angle of 30° and a cohesion of 100 kPa is 200 kPa. As can be seen from Figure 3.10 similar stress-strain curves are obtained for the unconfined test and the triaxial test under a confining pressure of 100 kPa. This gives us some confidence to consider cohesive soil in the numerical calculations.

3.4 Simulation of a biaxial test

3.4.1 Problem statement

Biaxial test is a test to study stress-strain behaviour in plane strain. The hypoplastic material properties are used from Table 3.5. The corresponding hypoplastic parameters are shown in Table 3.6.

Table 3.5: Material parameters used in the biaxial test

E [MPa]	μ [-]	ψ [°]	ϕ [°]	c [kPa]
30	0.2	5	25	0

Table 3.6: Corresponding coefficients of hypoplastic model

c_1	c_2	c_3	c_4
-83.3	-1369.3	-175.5	-316.7

Initially, the specimen is in an isotropic stress state. The test is carried out with constant confining pressure and simulated by applying a vertical velocity at the boundary while keeping the lateral stress constant.

3.4.2 FLAC3D model

The specimen is modelled as one single zone with unit dimensions (Figure 3.4). Initially, the model is fixed in the z-direction. A constant lateral confining pressure of 100 kPa is applied to the boundary faces between x = - 0.1 m and 0.1 m, x = 0.9 m and 1.1 m of the model in x-direction. A constant velocity of 1 × 10^{-6} m/step is applied to the boundary face located at z = 1 of the model in the negative z-direction, for a total of 50000 steps. The displacement is fixed in the y-direction during the test.

For comparison, the Mohr-Coulomb model is used to simulate the biaxial test too. The simulation procedure is similar with the simulation using hypoplastic model and will not be repeated here..

3.4.3 Numerical results

Figure 3.11 shows the numerical results of the biaxial test using hypoplastic model. The numerical results of the biaxial test using the hypoplastic model and the Mohr-Coulomb model are shown in Figure 3.12.

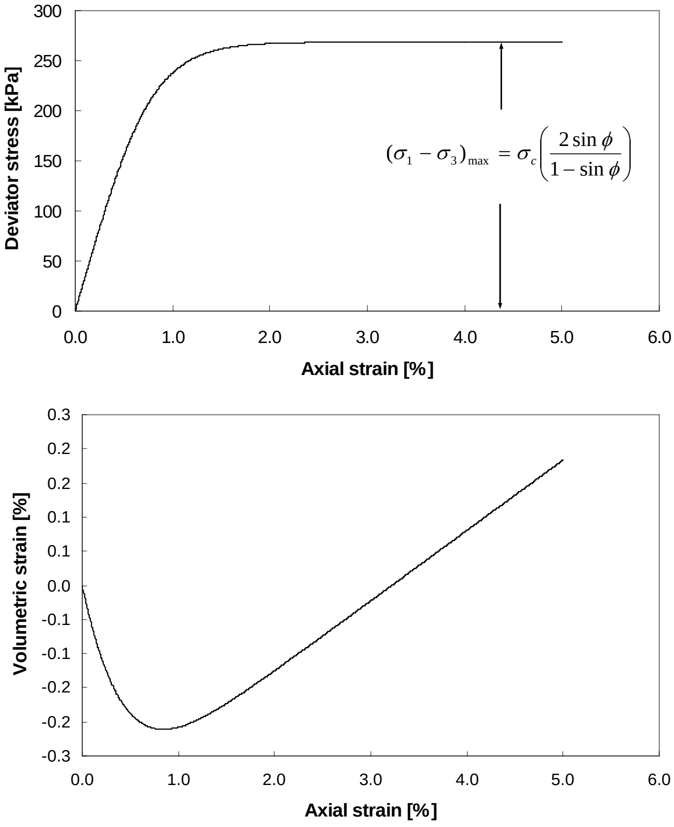

Figure 3.11: Numerical results of biaxial test

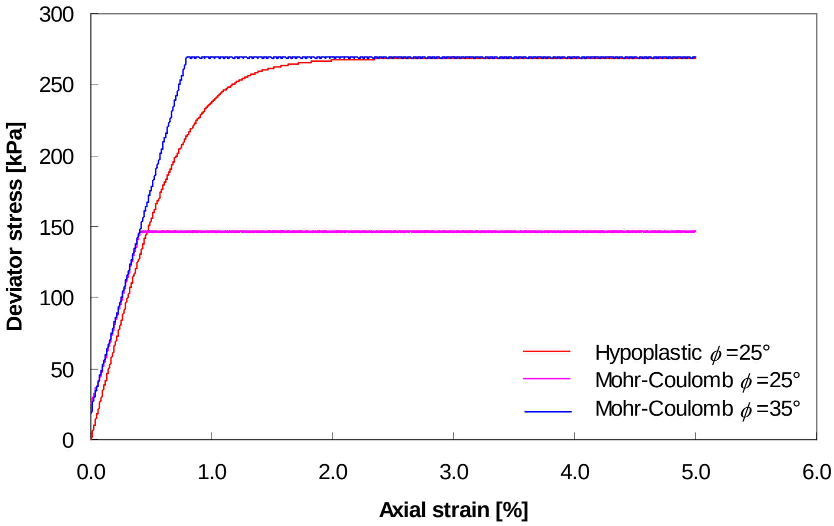

Figure 3.12: Comparison of numerical results of the biaxial test between hypoplastic model and Mohr-Coulomb model

The following observations can be made from Figure 3.12. The hypoplastic model gives rise to higher strength compared to the perfectly plastic model with Mohr-Coloumb failure criterion. The hypoplastic model assumes a Drucker-Prager failure criterion, which shows higher strength in plane strain than in triaxial compression. Some previous studies have shown that the present elastoplstic model with the Mohr-Coulomb failure criterion underpredicts the shear strength of sand in the biaxial mode of planar deformation ([11]). As mentioned at Section 2.3.2, the four coefficients of hypoplastic constitutive mode are related to the Young's Modulus E, the initial Poisson's ratio μ, the friction angle ϕ and the dilatancy angle ψ which are obtained from a single triaxial compression test. It is known that the friction angle in a triaxial test depends on the stress path. The friction angle of hypoplastic material in the biaxial test can be calculated from the simulation results. As shown in Figure 3.11 the confining pressure used in simulation is 100 kPa and $(\sigma_1 - \sigma_3)_{max}$ is about 270 kPa (the red line); then we have $\sin\phi = 2.7/(2.7+2) = 0.5745$ and the friction angle ϕ is about 35° in the biaxial test. As shown in Figure 3.12, the Mohr-Coulomb model with the friction angle of 35° (the blue line) predicts the same strength comparing with the hypoplastic model using the friction angle of 25° (the red line).

3.5 Simulation of simple shear test

3.5.1 Problem statement

Simple shear test is an improvement in relation to the direct shear because the specimen undergoes homogeneous strain. The test is conducted by applying a normal stress in oedometric conditions, then a shear stress is applied and distortions take place until the specimen fails (Figure 3.13).

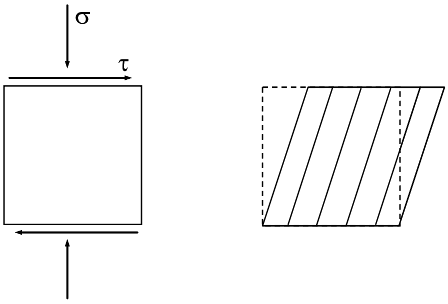

Figure 3.13: Stresses and deformation in a simple shear test

3.5.2 FLAC3D model

Two numerical simulations are carried out to show that the number of zones has no effect on the numerical results. In the first simple shear test, the specimen is modelled as one single zone with unit dimensions (Figure 3.4). The properties of material are shown in Table 3.7. The corresponding coefficients of hypoplastic model are shown in Table 3.8.

Table 3.7: Material parameters used in the first simple shear test

E [MPa]	μ [-]	ψ [°]	ϕ [°]	c [kPa]
20	0.2	10	35	0

Table 3.8: Corresponding coefficients of hypoplastic model

c_1	c_2	c_3	c_4
-47.23	-455.14	-112.17	-128.36

Initially, the model is in the compressive stress state. The model is fixed at the boundary face z = 0 in x-, y-, z-direction. The boundary faces between y = - 0.1 and y = 0.1, y = 0.9 and y = 1.1, x = - 0.1 and x = 0.1, x = 0.9 and x = 1.1 are fixed in y-direction. A constant confining pressure of 100 kPa is applied at the boundary face between z = 0.9 and z = 1.1 in the negative z- direction. The shearing process is simulated by applying velocities which varied from the zero at the bottom of the sample (z = 0) to the maximum at the top of sample (z = 1) in the positive x-direction. A total of 1800000 steps are simulated. The maximum velocity magnitude of 0.5×10^{-7} m/step is used.

The second simple shear test is carried out on a rectangle soil specimen of 120 mm × 40 mm × 10 mm (x × y × z). The geometry and the boundaries conditions in the second simple shear test are shown as Figure 3.14. The specimen is confined laterally with two rigid plates; each plate has a hinge at the bottom which allows rotation of the plate at the base of the specimen. The material properties are shown in Table 3.9. The corresponding coefficients of hypoplastic model are shown in Table 3.10.

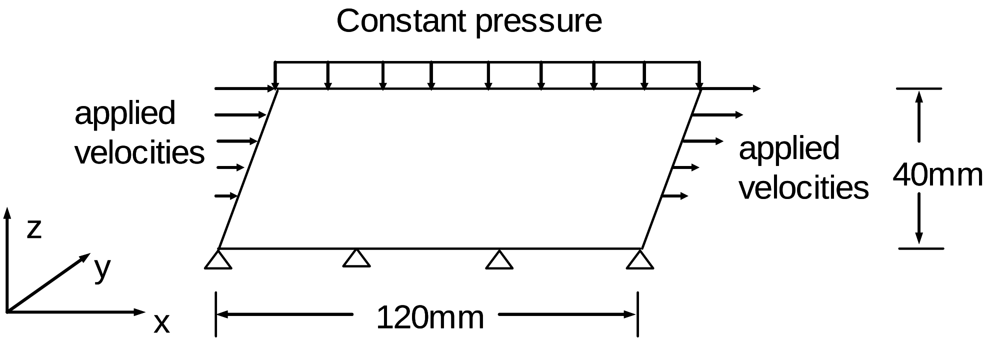

Figure 3.14: Geometry and boundaries conditions for the second simple shear test

Table 3.9: Material parameters used in the second simple shear test

E [MPa]	μ [-]	ψ [°]	ϕ [°]	c [kPa]
15	0.3	5	32	0

Table 3.10: Corresponding coefficients of hypoplastic model

c_1	c_2	c_3	c_4
-38.46	-406.22	-256.28	-112.36

The FLAC3D model for the second simple shear test is shown in Figure 3.15. The model is fixed at bottom in x-, y-, and z-direction. Because this test is considered as a plane-strain problem, the boundary faces at x = 0, x = 0.12, y = 0 and y = 0.01 of the sample are fixed in y-direction. Initially, an isotropic compressive stress 100 kPa is prescribed to the model, and a constant lateral confining pressure 100 kPa as the normal stress is imposed at the boundary faces located between z = 0.039 and 0.041. The top boundary at z = 0.04 of the model is free to move in both x- (horizontal) and z- (vertical) directions. The shearing process is simulated by applying velocities which varied from the zero at the base (z = 0) of the sample to the maximum at the top (z = 0.04) of the model in the positive x-direction. A total of 120000 steps is simulated with the maximum velocity magnitude of 0.2×10^{-7} m/step are used. The resultant of shear force vs. shear strain is plotted.

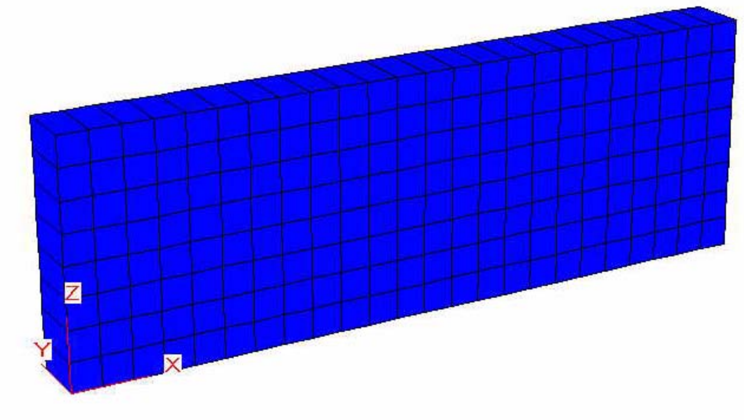

Figure 3.15: Model grid in FLAC3D for the second simple shear test

3.5.3 Numerical results

The numerical result of the first simple shear test is shown in Figure 3.16. The stress ratio σ_{12}/σ_{22} presents the ratio between the shear stress and the normal stress on the horizontal plane, namely the boundary face at z = 1 of the model.

The numerical result of the second simple shear test is shown in Figure 3.17. Figure 3.18 shows the deformed grid.

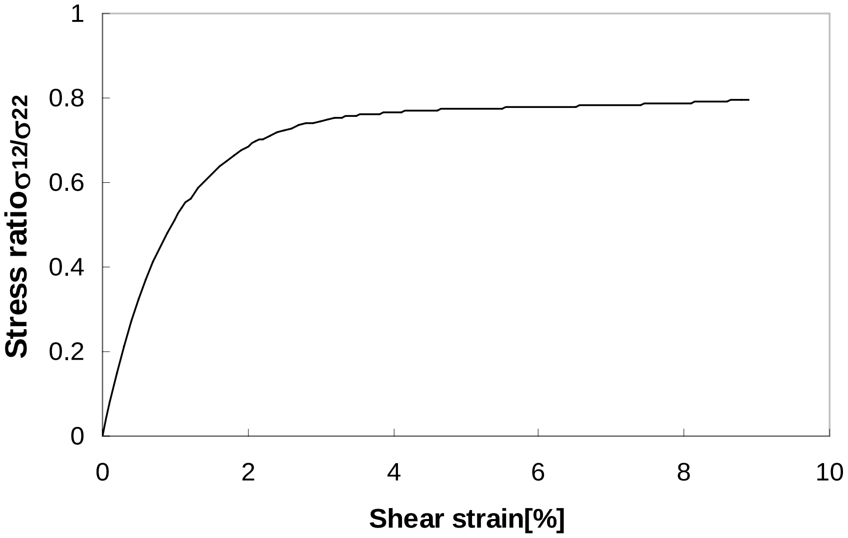

Figure 3.16: Numerical results of the first simple shear test

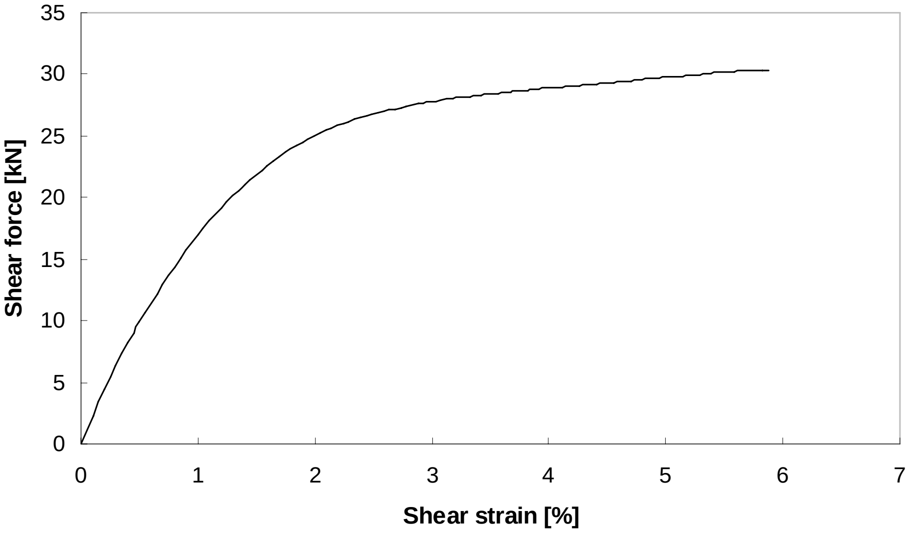

Figure 3.17: Numerical results of the second simple shear test

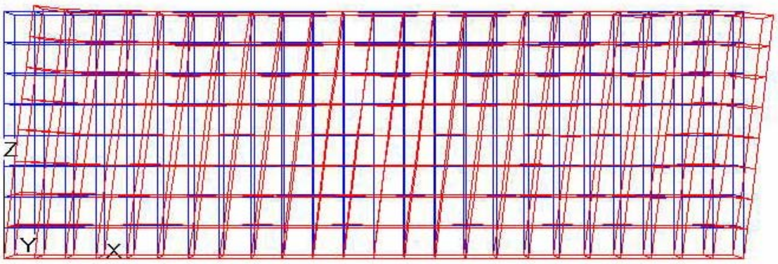

Figure 3.18: Deformed grid

From the deformed grid (Figure 3.18), it can be seen that small curvatures appear at both top corners of the model. This differs from the boundary conditions in laboratory test, where the normal stress is applied through a rigid platten. The rigid platten enforces the same displacement across the whole upper boundary. In the numerical simulation, however, a constant surface pressure is applied. A uniform pressure does not give rise to uniform dilatancy. It is likely that the stress distribution under the rigid platten is not uniform either. It seems impossible to obtain both uniform pressure and uniform dilatancy.

Chapter 4

Further Numerical Simulation Examples

This chapter studies the influences of the five parameters Young's Modulus, friction angle, dilation angle, cohesion and Poisson's ratio on the prediction of ground surface settlement of a shallow tunnel. For simplicity the tunnel cross-section is assumed to be circular. The hypoplastic model is used to simulate excavation and support and the numerical results are compared with numerical results obtained from the Mohr-Coulomb model.

4.1 Parameter study for a circular tunnel

4.1.1 Problem statement

The materials properties entering the hypoplastic model are to be determined via laboratory tests and their determination is subjected to different degrees of uncertainty. Therefore it is important to study the effect of these parameters on boundary value problems. Bofore the tunnel project will be dealt with in the next chapter, the effect of these parameters on the surface settlement is investigated. As mentioned before, the hypoplastic constitutive model involves five material properties, i.e. Young's modulus E, friction angle ϕ, Poisson's ratio μ, dilation angle ψ and cohesion c. In this study, a circular tunnel with 2 m diameter is simulated. The overburden above the tunnel crown is assumed to be 5 m.

4.1.2 FLAC3D model

Figure 4.1 shows the simple circular tunnel model grid in FLAC3D. The model tunnel is defined as 5 m long in the y-direction (Figure 4.1). The height of the model is 12 m and the width of the model is 20 m. The cutlength of the excavation is 1 m. Because of the objective of this study, the support measures (shotcrete lining and steel anchors) are not considered in this study. The ground surface settlement and tunnel closure are monitored during excavation. These values are recorded at the end of each excavation step. There are two cross sections selected to record the transverse trough profiles (section TL1m and section TL3m shown in Figure 4.1). A total of 5 sequential excavation steps are performed. Each excavation step is run for 4000 cycles to reach an equilibrium state.

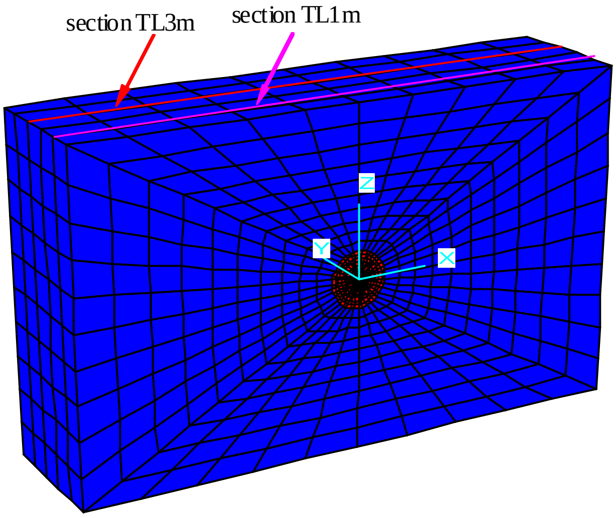

Figure 4.1: Model grid of the tunnel

4.1.3 Numerical results

1. Influence of Young's modulus

In this simulation, the parameters of the hypoplastic model are used from Table 4.1. Two Young's moduli are selected for this study, i.e. 20 MPa and 60 MPa. Other parameters remain unchanged for both simulations.

Table 4.1: Material parameters for the influence study of Young's modulus

E [MPa]	μ [-]	ψ [°]	ϕ [°]	c [kPa]
20/60	0.3	5	25	5

The numerical result of longitudinal settlement trough for different Young's modulus is shown in Figure 4.2. Figure 4.3 and Figure 4.4 show the numerical results of transverse troughs for different Young's modulus. The numerical results in the above figures are obtained at the end of the five excavation steps.

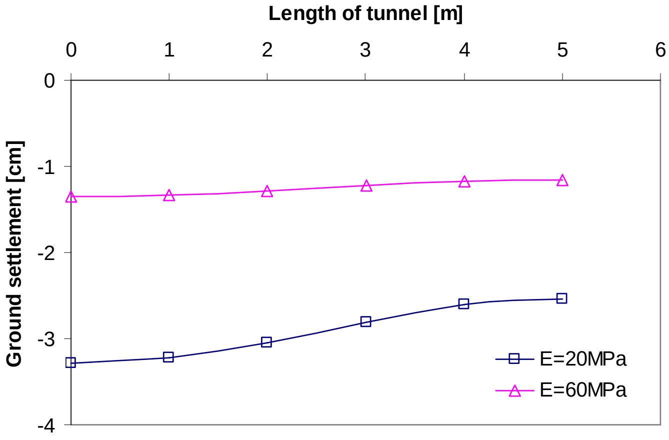

Figure 4.2: Numerical results of longitudinal settlement for different E

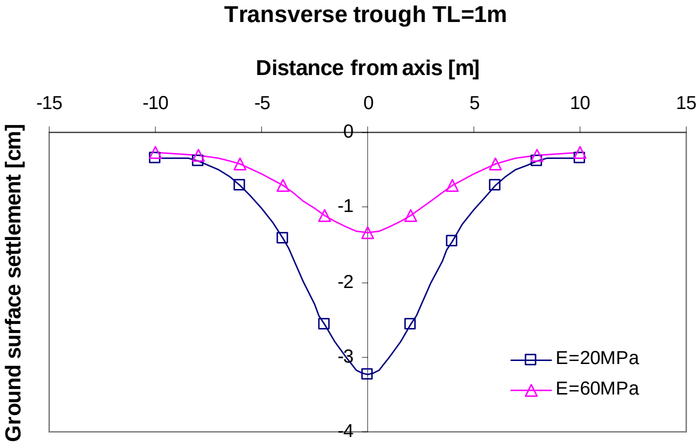

Figure 4.3: Numerical results of transverse trough of section TL1m for different E

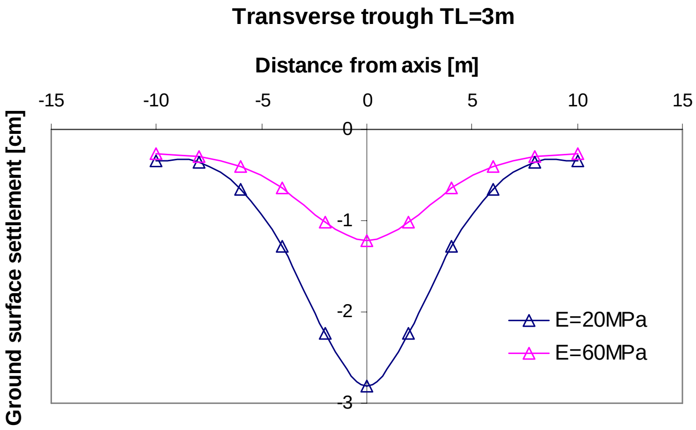

Figure 4.4: Numerical results of transverse trough of section TL3m for different E

The difference between the longitudinal settlements for Young's modulus of 20 MPa and Young's modulus of 60 MPa is about 60 %, indicating the importance of influence of variation of the Young's modulus. Figure 4.3 and Figure 4.4 show that increasing of Young's modulus leads to shallower ground surface settlement however, the width of transverse trough seems not to be influenced by Young's modulus. There is minor difference between the maximum settlement at TL1m and TL3m.

2. Influence of friction angle

The material parameters to study the influence of friction angle are shown in Table 4.2.

Table 4.2: Material parameters for the influence study of friction angle

E [MPa]	μ [-]	ψ [°]	ϕ [°]	c [kPa]
30	0.3	5	22/27/32	5

The numerical results of longitudinal settlement for different friction angles are shown in Figure 4.5. Figure 4.6 and Figure 4.7 show the numerical results of transverse troughs for different friction angles.

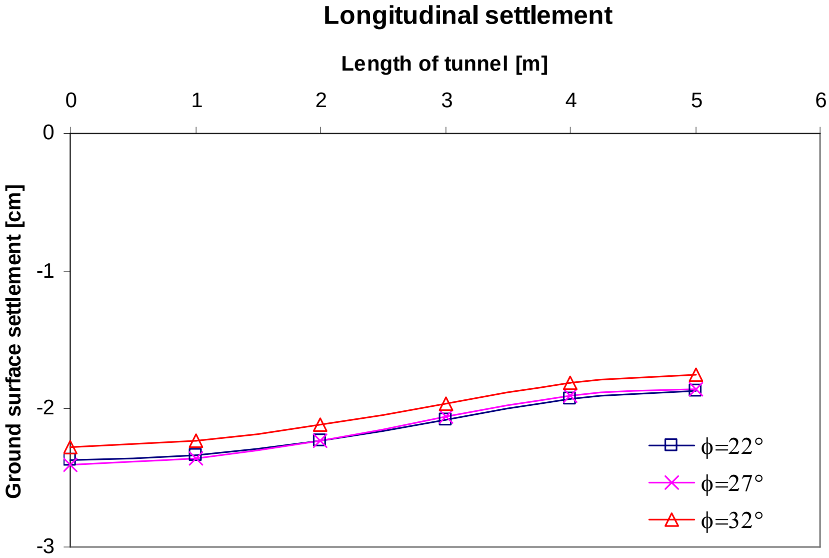

Figure 4.5: Numerical results of longitudinal settlement for different ϕ

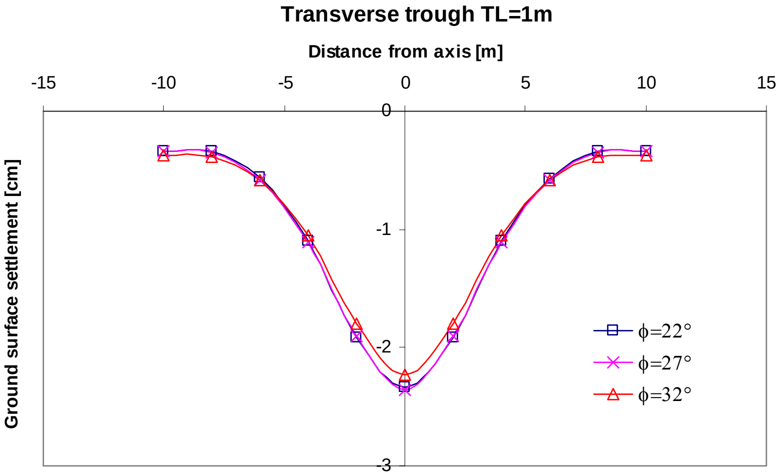

Figure 4.6: Numerical results of transverse trough of section TL1m for different ϕ

Figure 4.5 shows that the difference of longitudinal settlement between the friction angle of 22° and 27° is not significant, and the difference between the longitudinal settlement with $\phi = 27°$ and 32° is only about 6 %. From Figure 4.6 and Figure 4.7, it can be seen that the transverse settlement trough with a friction angle of 32° is somewhat shallower than the transverse trough with friction angle of 22° and 27°. However, the difference is minor. The numerical results show that the influence of friction angle on the ground surface settlement is not significant.

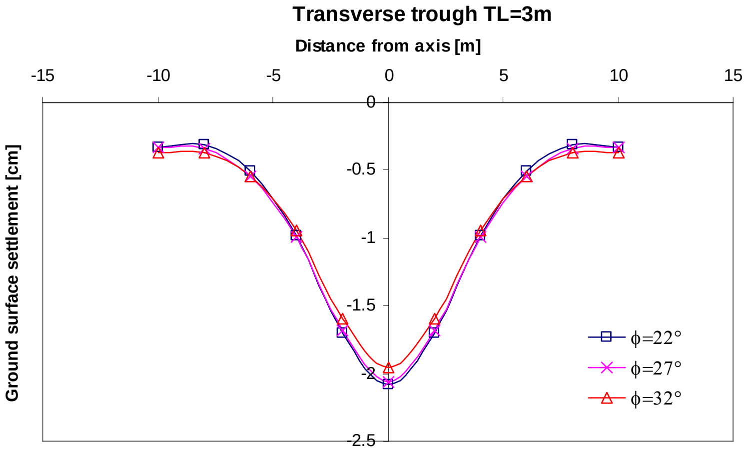

Figure 4.7: Numerical results of transverse trough of section TL3m for different ϕ

3. Influence of Poisson's ratio

Poisson's ratio for soils may vary between 0 and 0.5. In this study, three Poisson ratios are selected as shown in Table 4.3.

Table 4.3: Material parameters for the influence study of Poisson's ratio

E [MPa]	μ [-]	ψ [°]	ϕ [°]	c [kPa]
30	0.1/0.3/0.4	5	25	5

The numerical results are shown in the following figures. Figure 4.8 shows the longitudinal settlement of the tunnel for the material with three different Poisson's ratios. Figure 4.9 and Figure 4.10 show the transverse trough profiles for different Poisson's ratios.

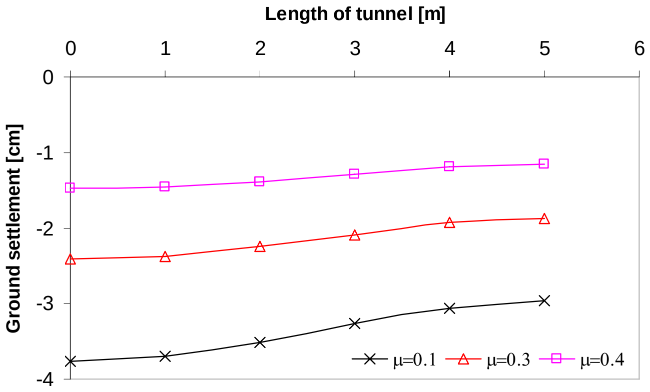

Figure 4.8: Numerical results of longitudinal settlement for different Poisson's ratios

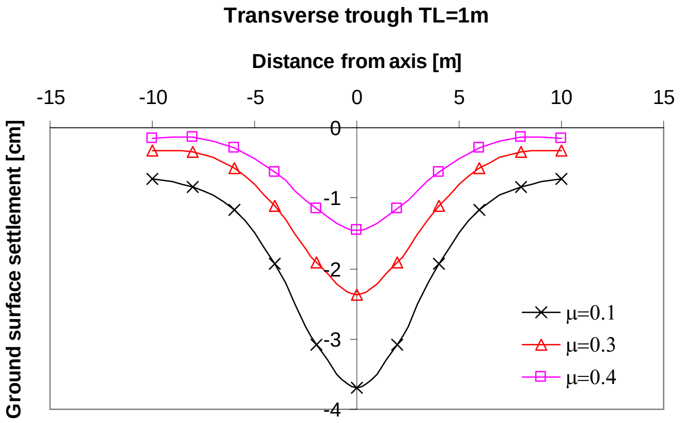

Figure 4.9: Numerical results of transverse trough of section TL1m for different Poisson's ratios

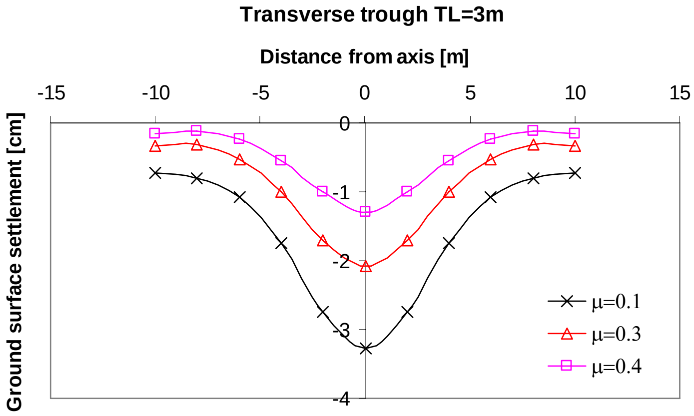

Figure 4.10: Numerical results of transverse trough of section TL3m for different Poisson's ratios

It can be seen from Figure 4.8, Figure 4.9 and Figure 4.10 that the variation of Poisson's ratio has significant influence on the ground surface settlement. Higher Poisson ratios give rise to larger surface settlement. The ground surface settlement above the tunnel axis reduces by about 36 % as the Poisson's ratio increases from 0.1 to 0.3. The ground surface settlement above the tunnel axis reduces by about 38 % as the Poisson's ratio increases from 0.3 to 0.4.

4. Influence of dilation angle

The parameters of material are used from Table 4.4 to study the influence of dilation angle.

Table 4.4: Material parameters for the influence study of dilation angle

E [MPa]	μ [-]	ψ [°]	ϕ [°]	c [kPa]
30	0.3	0/10	25	5

The numerical results are shown in Figure 4.11, Figure 4.12 and Figure 4.13.

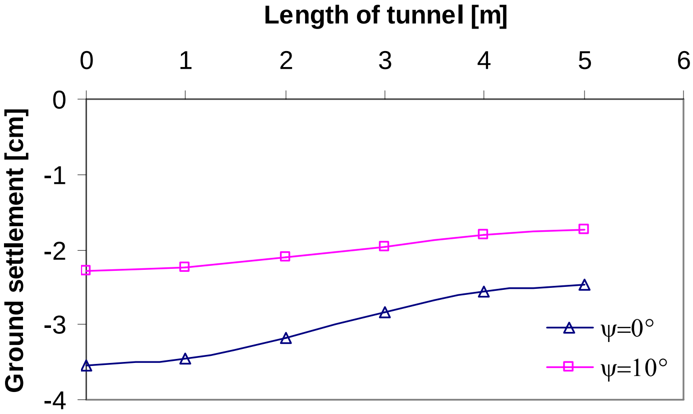

Figure 4.11: Numerical results of longitudinal settlement for different dilation angles

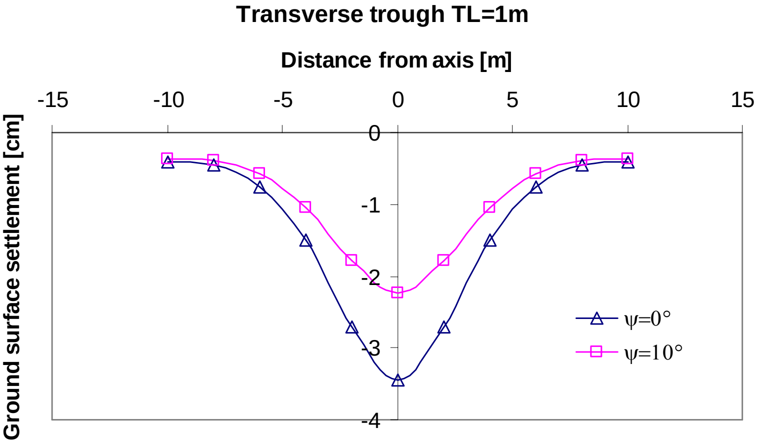

Figure 4.12: Numerical results of transverse trough of section TL1m for different dilation angles

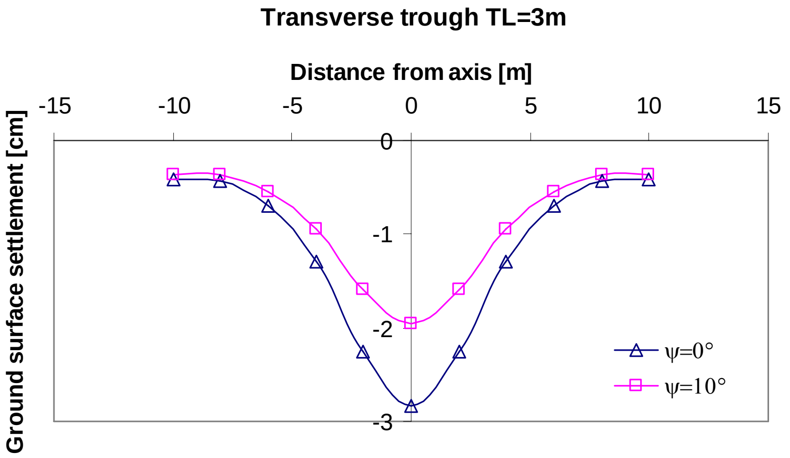

Figure 4.13: Numerical results of transverse trough of section TL3m for different dilation angles

The longitudinal settlement reduces by about 35 % between as the dilation angle increase from 0 to 10° (see Figure 4.11). As Figure 4.12 and Figure 4.13 shown, increasing of dilation angle leads to the shallower transverse trough while does not affect the width of transverse trough.

5. Influence of cohesion

The material parameters to study the influence of cohesion are given in Table 4.5.

Table 4.5: Material parameters for the influence study of cohesion

E [MPa]	μ [-]	ψ [°]	ϕ [°]	c [kPa]
30	0.3	5	25	1/5

The numerical results of the influence study of cohesion are shown in Figure 4.14, Figure 4.15 and Figure 4.16.

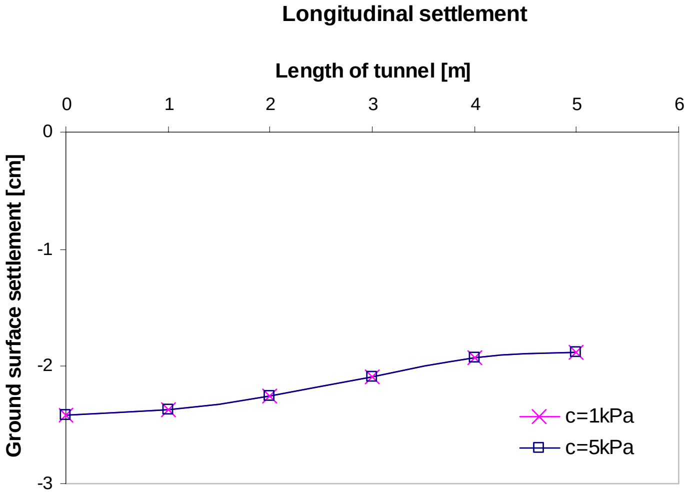

Figure 4.14: Numerical results of longitudinal settlement for different cohesion

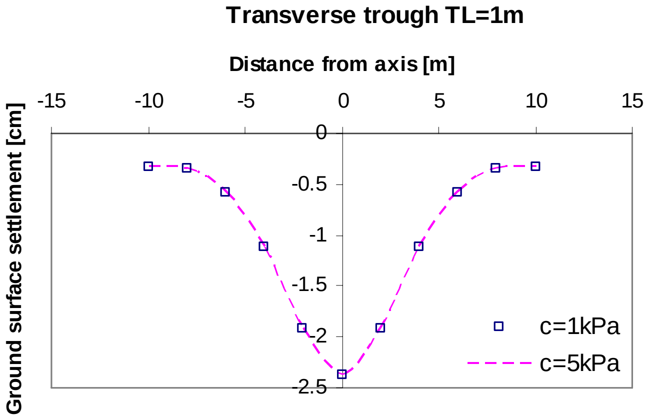

Figure 4.15: Numerical results of transverse trough of section TL1m for different cohesion

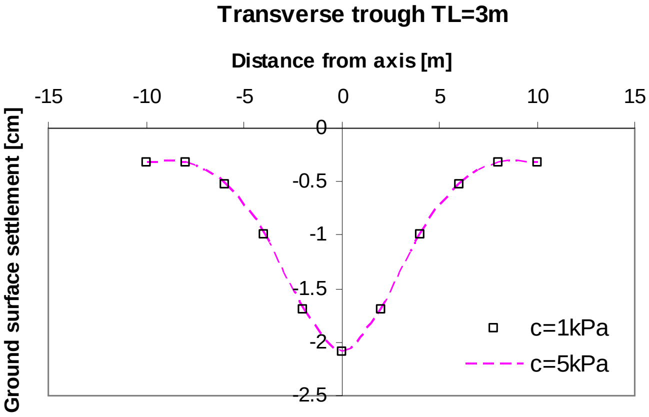

Figure 4.16: Numerical results of transverse trough of section TL3m for different cohesion

From Figure 4.14 it can be seen that the influence of variation of cohesion on the longitudinal settlement is minor. The same conclusion can be obtained based on Figure 4.15 and Figure 4.16.

4.1.4 Summary

Based on the results from the previous section, the following summaries can be made:

First, the variations of friction angle and cohesion have minor influences on the prediction of ground surface settlements. These two parameters can be derived from laboratory tests. However these two properties measured in laboratory can not represent the real properties in the filed sometimes. It indicates that friction angle and cohesion have high uncertainties. Based on this study results, it can be concluded that the uncertainties of friction angle and cohesion will not produce negative effects on the numerical analysis.

Second, dilation angle's change has significant influence on the prediction of ground surface settlements. About dilation angle, it is already known that it is generally significantly smaller than the friction angle for soils, rocks and concrete. Vermeer and de Borst (1984) observe that values for the dilation angle are approximately between 0° and 20° whether the material is soil, rock, or concrete. Some typical values for dilation angle are reported too; so basically dilation angle has low uncertainty as property of material. It means that the influence of dilation angle in numerical analysis is limited.

Third, the variation of Poisson's ratio has noticeable influence. Like dilation angle, Poisson's ratio as one of properties of material has been well known. The uncertainty of Poisson's ratio is kind low. This would limit the influence of Poisson's ratio in numerical analysis.

Fourth, the numerical results show that the variation of Young's modulus has significant influence on the prediction of ground surface settlements. Young's modulus is one of most important properties in engineering design. However Young's modulus can vary somewhat due to differences in sample composition and test method. It means that the value of Young's modulus has high uncertainty. So, Young's modulus need to be paid attention whenever in numerical analysis or in engineering design.

4.2 Simulation of excavation and support for a shallow tunnel

4.2.1 Problem statement

The numerical calculations in the last section have been carried out to study the influence of some material parameters on the surface settlement. The problem there has been idealized, e.g. without considering support, and therefore does not represent real tunnelling situations. In this section we proceed to simulate some support measures in our calculation. We consider a shallow tunnel in soft ground in urban area. The tunnel is constructed according to the New Austrian Tunnelling Method with a primary shortcrete lining and a final cast in-place concrete liner. It is important to minimize the impact of tunnelling on surface structures. Surface settlements depend on both excavation method and tunnel support. The surface settlement resulting from an advancing tunnel is three dimensional and ought to be treated as such.

The construction method of this tunnel uses a combination of support measures to reinforce. The components of the construction method are (as shown in Figure 4.17):

a. Excavation of a 3 m cut;

b. Installation of steel arch support immediately behind the excavation face;

c. Construction of a 4 m long, 22 cm thick angled slot above the tunnel and filled with concrete to act as a pre-support shield;

d. Installation of a shotcrete lining between steel support; and

e. Installation of horizontal cable bolts in the tunnel face.

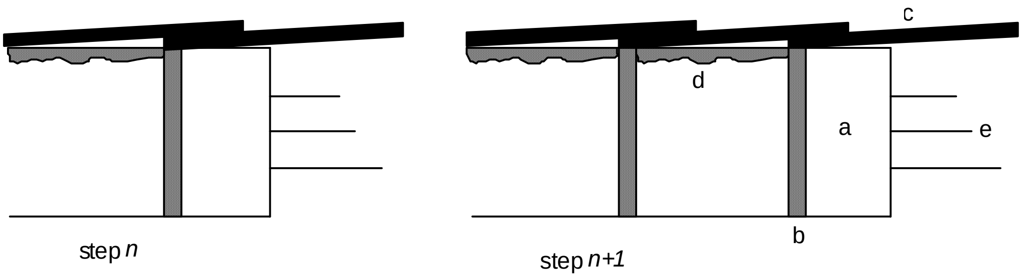

Figure 4.17: Components of the tunnel support method

A thick concrete liner is installed behind the advancing tunnel face. Figure 4.17 shows the components of the method. In order to evaluate the influence of the support method on surface settlement, every component should be simulated by the numerical analysis.

4.2.2 FLAC3D model

The tunnel model with a length of 51 m is shown the following figure. By making use of the symmetry, only one-half of the tunnel is modelled. The base of the tunnel is located at about 39.5 m below the ground surface. The tunnel crosssection consists of a half circle with a radius of 5 m. A system of coordinate axes is defined with the origin at the floor of the tunnel; the z-axis points upward and the y-axis points along the axis of the tunnel (see Figure 4.18). The soil properties are shown in Table 4.6.

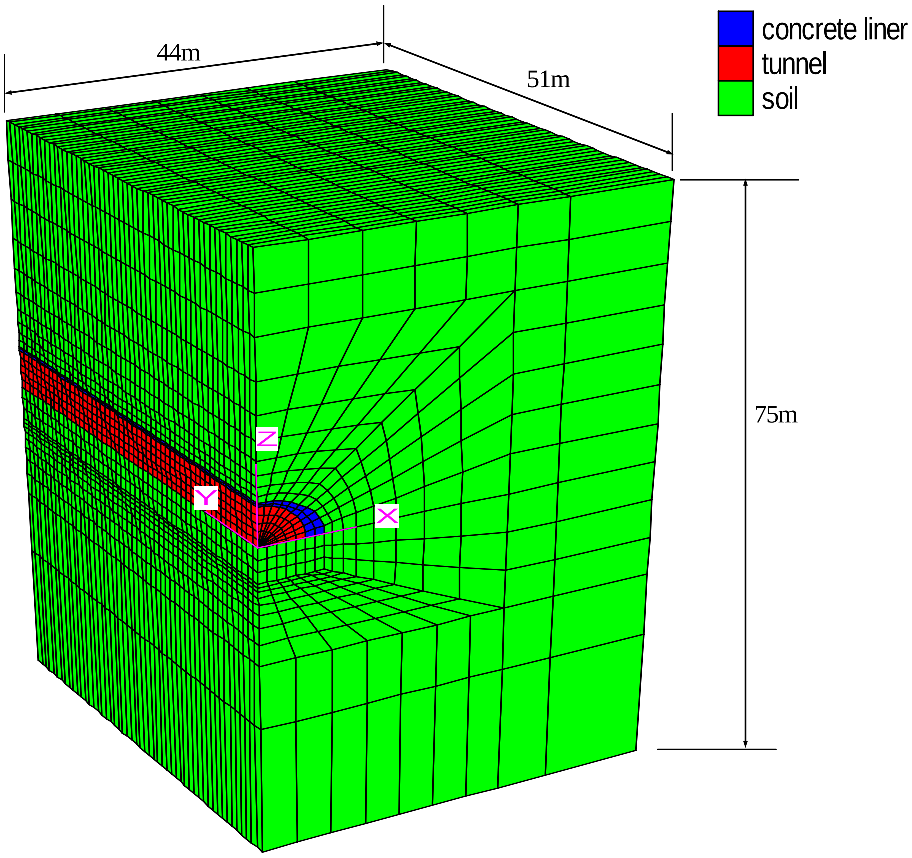

Figure 4.18: Model grid of the tunnel in FLAC3D

Table 4.6: Material parameters

E [MPa]	μ [-]	ψ [°]	ϕ [°]	c [kPa]
30	0.3	5	25	5

The initial stress state obtained through gravitational loading with the following relation between vertical and horizontal stresses: $\sigma_{zz} = \sigma_{xx} = 2\sigma_{yy}$, which corresponds to an earth pressure coefficient at rest of 0.5.

The primary shotcrete lining has a thickness of 30 cm and is modelled with shell structural elements because of its small thickness(see Figure 4.19). The final concrete lining has a thickness of about 1.5 m and is modelled with zones because of its large thickness. The liners are assumed to be elastic with an elastic modulus of 31.4 GPa and a Poisson's ratio of 0.25. The horizontal cable bolts installed at the tunnel face are modelled with cabel structural elements with modulus of 45 GPa, cable area of 1.57×10^{-3} m^2, tensile capability of 250 kN, bond stiffness of 17.5 $\times 10^6$ N/m/m and cohesive strength of 2 $\times 10^4$ N/m^3.

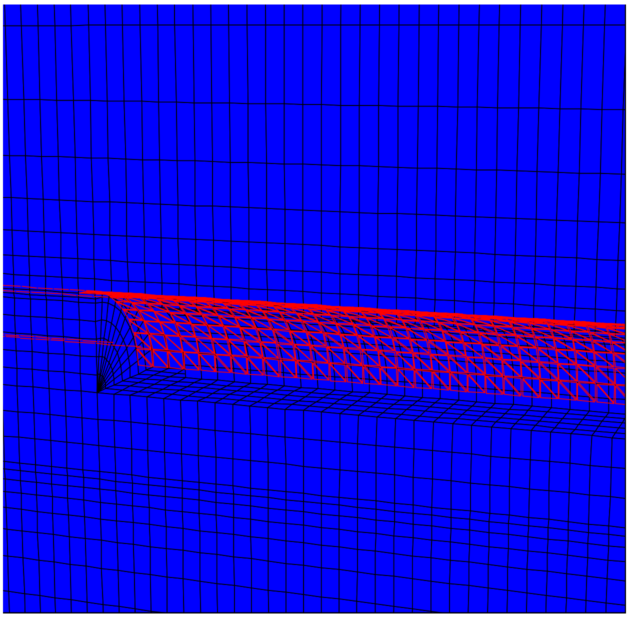

Figure 4.19: Structural elements (shells and cables)

The tunnel is constructed in two phases (top heading followed by invert excavation and support). First, the upper, arched portion of the tunnel is excavated and supported. Then, the lower portion of the tunnel is excavated and supported. In this example, only the first stage analysis is illustrated; the second stage construction would follow the same procedure.

The excavation and support installation are conducted incrementally with an excavation length of 3 m. The shotcrete lining is installed immediately after the excavation. The final liner is installed 3 m behind the excavation face. A combination of 9 m, 12 m and 15 m length bolts are installed. The bolt installation process uses (alternatively) three different bolt patterns. In the simulation, a FISH function **excav** is used to control the excavation and support installation process. In order to install a continuous lining with the shell elements, the shell element is given the same identification number as the existing shell element from the previous step. The new shell element will then use the existing nodes at the existing shell. The new shells have zero stresses initially.

A total of fifteen sequential excavation and support steps are performed. Each construction step needs some 3000 cycles to reach an equilibrium state. The ground surface settlement and tunnel closure are registered throughout the calculation. The ground surface settlements are recorded at two tunnel stations, i.e. TL15m and TL30m these two positons lie 15 m and 30 m from the tunnel portal respectively. The transverse troughs of these two cross sections are presented.

4.2.3 Numerical results

The numerical results are shown in the following figures. For comparison, the numerical results using the Mohr-Coulomb model are presented too. The settlement troughs in these figures are calculated for two excavation stages, i.e. *excav=15 m* and *excav = 30 m*, i.e. when the excavation reaches 15 m and 30 m from the portal.

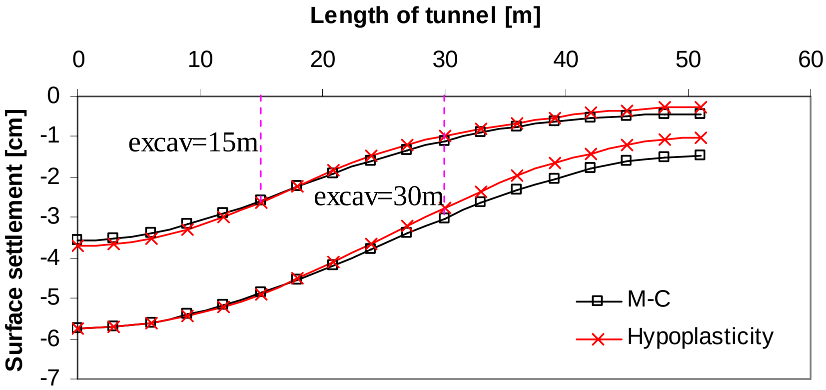

Figure 4.20: Numerical results of longitudinal settlements

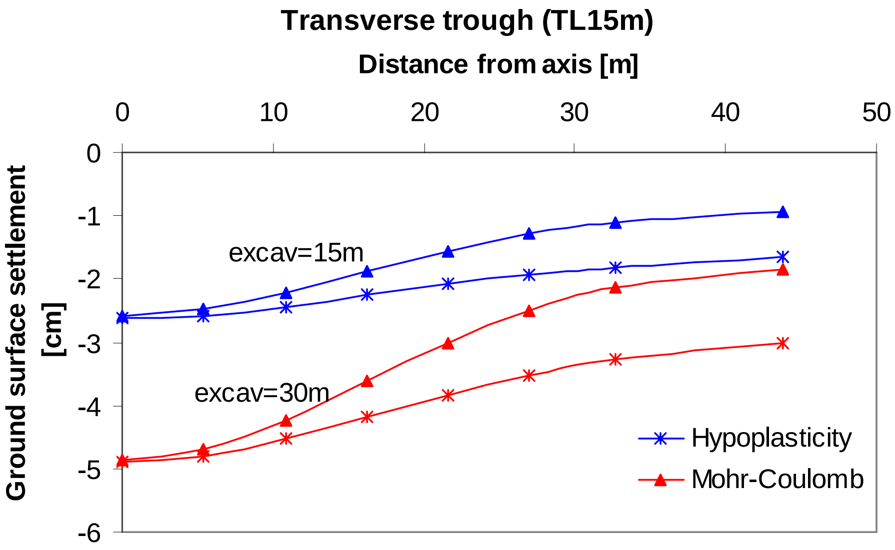

Figure 4.21: Numerical results of transverse troughs of cross section TL15m

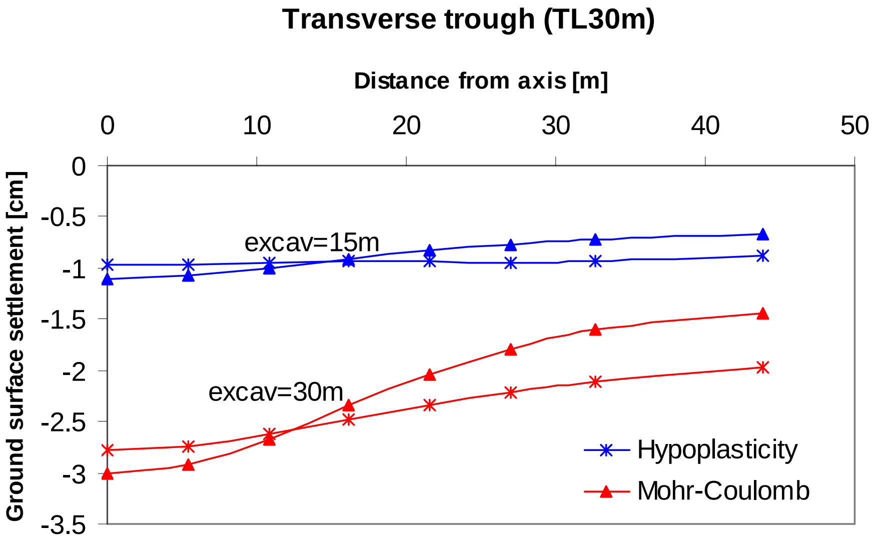

Figure 4.22: Numerical results of transverse troughs of cross section TL30m

As can be seen from Figure 4.20, the longitudinal settlement troughs obtained with the hypoplastic model agree well with those with the Mohr-Coulomb model. The numerical results of transverse troughs (see Figure 4.21 and Figure 4.22) show that the difference between the maximum settlements predicted by both models is very, however the transvers troughs predicted by hypoplastic model are wider than those predicted by the Mohr-Coulomb model.

Chapter 5

Numerical Simulation of a Shallow NATM Tunnel

The implementation of the hypoplastic model has been verified for different problems in the last chapter, which gives us some confidence in simulating real tunnels with our model. In this chapter a tunnel under construction is simulated and the numerical results are compared with measurements. The Lainzer tunnel is a twin-track railway tunnel of about 12.8 km long in Vienna. It is part of the European high-speed rail-link between Paris and Budapest. It is a shallow tunnel in urban area. It is constructed according to NATM (New Austrian Tunnelling Method). Besides the conventional support measurements, a special advancing reinforcement by horizontal glass fibre anchors (GFK) is used. Therefore a trial field is established where the new method is tested. In this study, the numerical program FLAC3D is used to simulate the construction of the Lainzer Tunnel. The numerical results obtained from hypoplastic model are compared with the measurements from this trial field.

5.1 New Austrian Tunnelling Method(NATM)

NATM (New Austrian Tunnelling Method) as the conventional tunnelling method was first introduced in the early 1960's. This method involves the use of shotcrete (sprayed concrete) and the systematic installation of anchors (or a number of further supporting means) to support the ground. The NATM is based on the following principles:

- To allow certain deformation in order to encourage the formation of a load carrying arch, which protects the excavation and reduces the final stress in lining;

- The use of sprayed concrete (shotcrete) immediately after excavation minimized risk of loosening and extensive rock deformation;
- Measuring the deformation with sophisticated measurement techniques embedded in lining, ground and boreholes;
- Flexible support, the shotcrete lining is thin and reflects the recent strata conditions. The support is used rather active than passive, enhancing the strength is not only achieved by thicker lining but by a flexible combination with rock bolts, wire mesh and steel rib;
- Closing the invert. Rapid ring closure stops ongoing deformation and activates the support;
- Contractual arrangements, since the NATM is based on monitoring measurements, changes in support and construction method are possible. The contract has to allow such changed in order to be more cost efficient or increase safety;
- Rock mass classification systems like RMR (Rock Mass Rating), Q-System can be used to determine support measures.

The advantage of NATM lies in its simplicity and flexibility. Originally developed for deep tunnels, NATM has become applicable also for shallow tunnels in soft soil ground. Excavating tools can be easily adapted to changing ground conditions, whether it is a roadheader for jointed rock, excavator shovel in soil or the drill and blast method for strong rock. The support measures of NATM are flexible and can be modified to almost any desired assembly. The ground investigation determines the excavation and support classes throughout the tunnel length depending on the expected ground behaviour.

Another major advantage of NATM is the possibility of excavating arbitrarily cross sectional geometries and longitudinal curves. In case of tough ground condition and large tunnel diameters, the cross section is usually divided in a number of partial faces. By this means a gentle treatment of the rock mass is guaranteed and the deformations even in difficult grounds remain bearable. Nowadays two typical methods of partial excavation are available: advancing top heading and driving in side galleries.

The advancing top heading is followed by the bench and completed by the invert closing the ring. The principles of NATM demand among others a quick closure of the invert. Usually the top heading should not advance more than $2 \sim 5$ cut length. Weak ground conditions or large tunnel diameter can require a temporary invert in the top heading in order to reduce excessive deformation. The aim of widening the footing so called elephant foot or improving the ground with micro poles is to reduce those settlements.

Driving in side galleries is a very gentle way of construction and is usually performed in weak ground conditions. The shape of the advancing side galleries are statically favorable for high vertical loads and will be used as abutments for the following top heading. The whole construction procedure is very laborious.

5.2 Geotechincal Information of Lainzer Tunnel

5.2.1 General Description

The Lainzer Tunnel is one of the most important projects now under construction as part of the Austrian high-speed Railway System. It is part of European high-speed rail-link between Paris and Budapest. It serves as the connection of Austrian Western Railway with Austrian Southern Railway and Donauländebahn Railway. When this project is completed, the single-track connection between the Southern and Western Austrian Railway shall be relieved. The whole project is implemented in four subsections namely, Interconnection to Western Railway, connecting tunnel, Connection to Donauländebahn Railway, and Integration to Southern Railway as shown in Figure 5.1.

The whole project is about 12.8 km long, a 12.3 km portion of which is being constructed as a railway tunnel. Starting from three access shafts, the construction works on the double-track tunnel with twelve safety exits are being carried ou.

The connecting tunnel part is concerned in this thesis. The connecting tunnel is further divided into three lots namely LT31, LT33 and LT44. The presented simulation is focused on LT31 (Figure 5.2), where the trial field is located. LT31 is about 3 km long. The excavation of LT31 lot began in 1996. According to schedule, the whole tunnel shall be completed by 2012. The height of tunnel is about 12.5 m. The overburden varies between 6.5 m and 26.5 m.

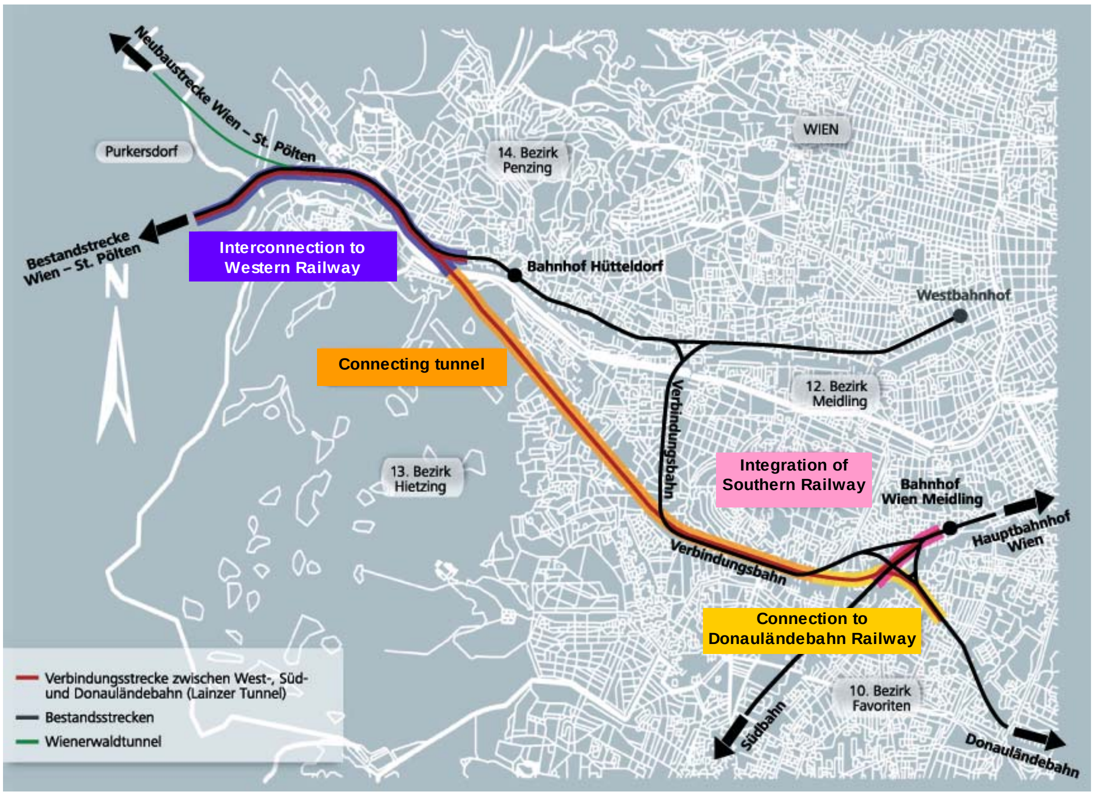

Figure 5.1: Project plan of the Lainzer Tunnel

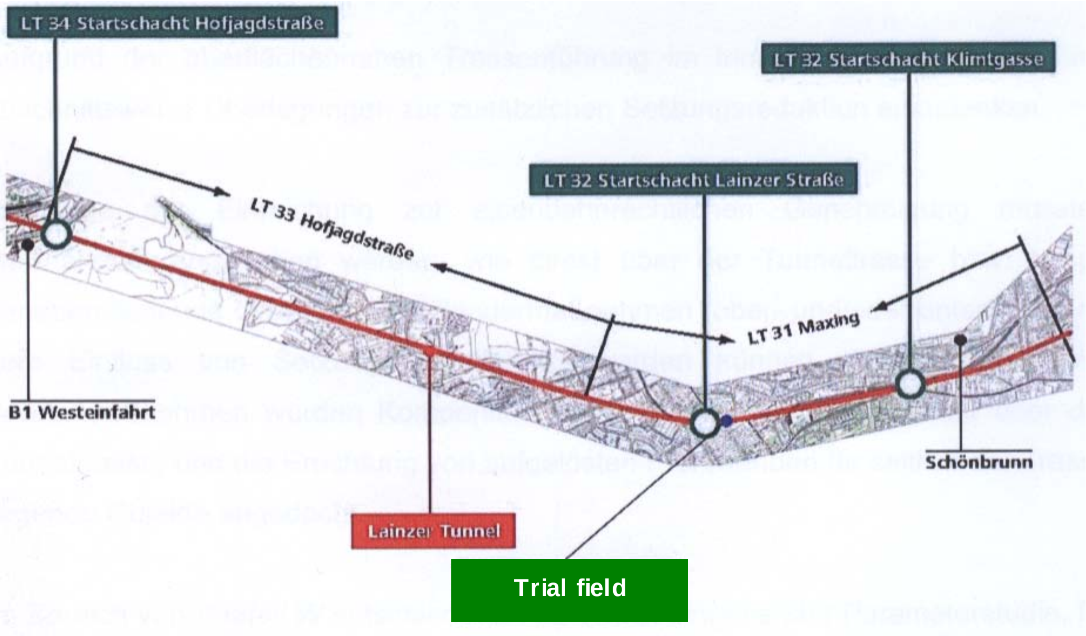

Figure 5.2: Subsections of the connecting tunnel

5.2.2 Geotechnical properties

The Lainzer Tunnel lies in tertiary strata of Vienna basin. Figure 5.3 shows the geology setting of LT31. The ground consists mainly of silt and clay. To define the ground properties, numerous laboratory tests including 54 uniaxial compressions tests and 14 triaxial tests were performed. According the geotechnical report, the ground is divided into twelve categories of similar geotechnical behavior ranging from strong conglomerate to silt and clay with inter-beddings of sand and gravel. The properties of the silt and clay are shown in Table 5.1.

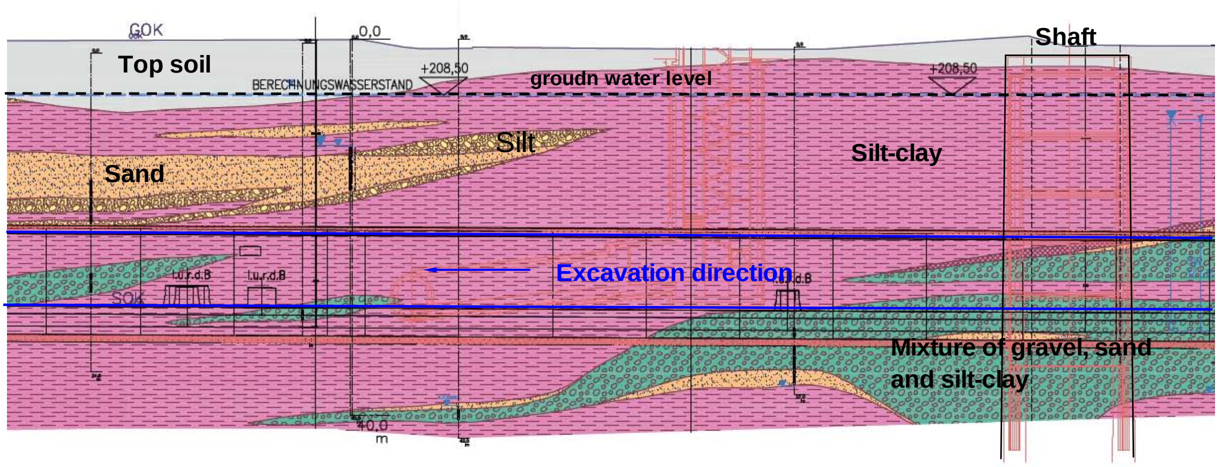

Figure 5.3: Geology setting of LT31 lot

Table 5.1: Properties of GA5 silt and clay

γ / γ' [kN/m^3]	ϕ [°]	c [kPa]	E_load [MPa]	E_unload [MPa]	E_reload [MPa]	μ [-]
20.5/11.0	23	60	40	150	80	0.4

5.2.3 Face support measures

The tunnel advance is started from two shafts and undergoes an urban area with numerous buildings above. In order to avoid damage to the buildings, strict settlement control is being used. Because of this sensitivity, besides the conventional face support measurements, a special advancing reinforcement by horizontal glass fibre anchors is used.

Figure 5.4 shows the two different face support schemes. The GFK support consists of some 26 $\sim$ 29 glass fiber anchors of 18 m length. An overlap of about 6 m is provided. The traditional face support consists of some 5 $\sim$ 6 steel anchors with a length of about 12 m. In this case, a face sealing of shotcrete and a load-distributing anchor head ensure the quality of face support. During tunnel excavation the anchor plates are cut off giving rise to some negative effect on displacement. The GFK anchors are based on the bound between anchor rod and ground and remain active all the time. The high installation density of about 0.8 anchor/m^2 aims at reinforcing the ground. Table 5.2 shows the propterties of the glass fibre anchors.

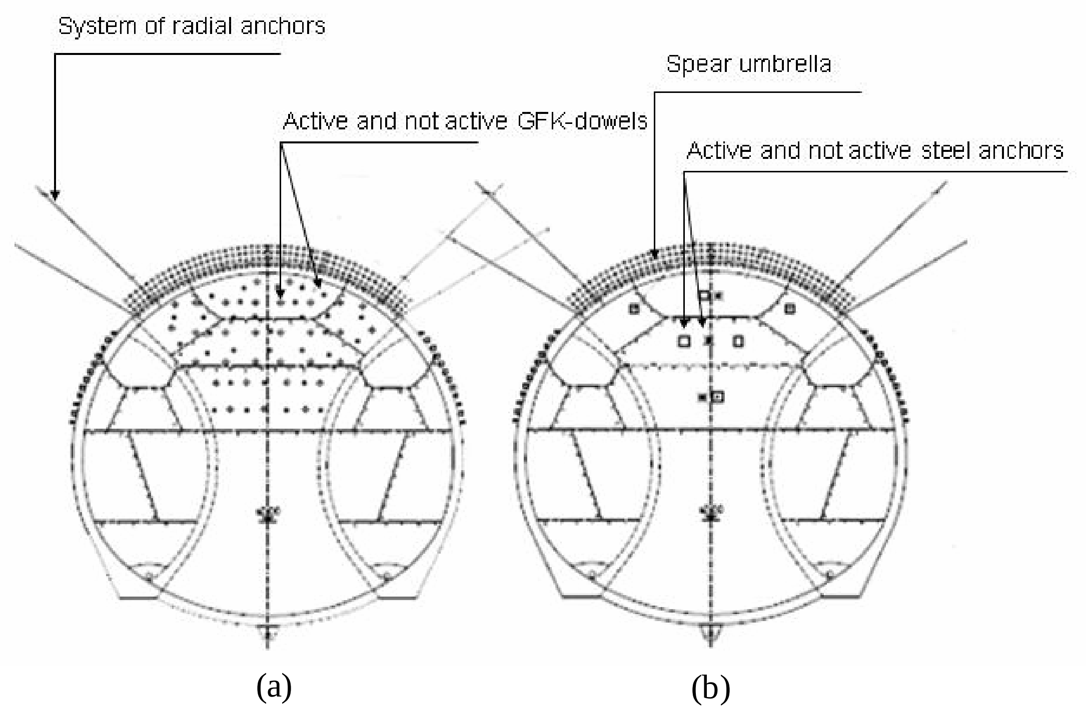

Figure 5.4: Two different face support schemes:(a) GFK anchors,(b) conventional steel anchors

Table 5.2: Properties of glass fibre anchors

Density [g/cm^3]	Glass content [%]	Tensile strength [GPa]	Shear strength [MPa]	E [GPa]	Failure strain [%]
1.9	70	1	200	40	> 3

5.2.4 Excavation scheme

The area of tunel crosssection is about 130 m^2. For sequential excavations, the tunnel cross section is divided into four parts with roughly equal area, i.e. two side galleries, Core_I and Core_II (Figure 5.5). In order to minimize the interaction between two subsequent excavations, the longitudinal distance between any two excavation faces shall not be less than 20 m. The enlarged footings (elephant footings) in Figure 5.5 aim to reduce the vertical settlements.

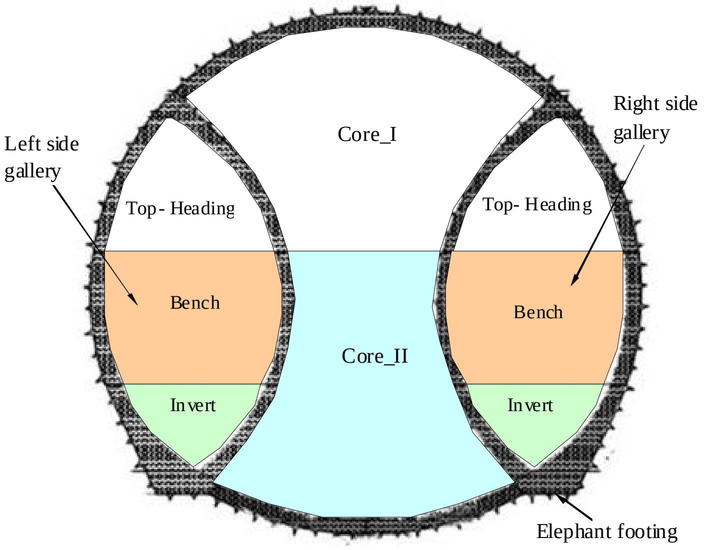

Figure 5.5: Cross section of Lainzer Tunnel

Excavation of side galleries

The side galleries are further divided into top heading, bench and invert as Figure 5.5 shown. The excavation of the side galleries in the longitudinal direction follows the following procedure: 1 m top heading excavation, 1m bench excavation; afterwards 1m top heading excavation, 1m bench excavation, and then 2 m invert excavation (see Figure 5.6). Two layers of steel mesh are incorporated within 30 cm of shotcrete, enabling it to sustain surcharge loads exerted by the constructions machines during the excavation.

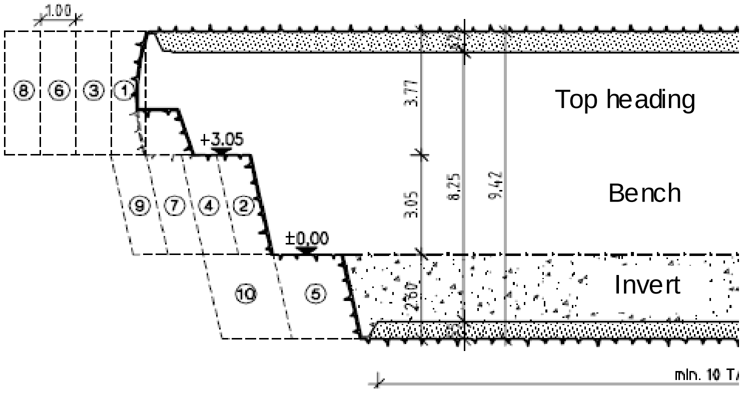

Figure 5.6: Excavation procedure of side gallery

Excavation of Core_I and Core_II

The excavation of Core_I was started after the advance face of the right side gallery was sealed. The longitudinal distance between these two advance faces must be at least 20 m. Figure 5.7 shows the excavation procedure of Core_I. The invert of Core_II was covered with the excavated material from Core_I as a ramp in order to let the construction machines pass through. The excavation of Core_II is shown in Figure 5.8. The Core_II was excavated with a 2 m cutlength, followed by the removal of the shotcrete (inner wall) of the side galleries. The installations of reinforced shotcrete in Core_ and Core_II followed the same procedure with them in side galleries. Besides that, the special face supproting by the horizontal glass fibre anchors was installed at advance face of Core_I (see Figure 5.4(a)).

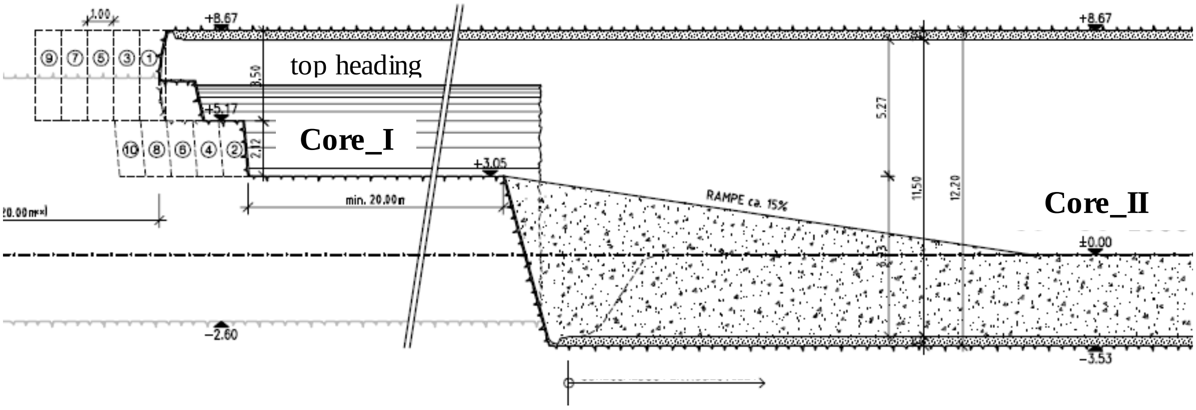

Figure 5.7: Excavation procedure of Core_I

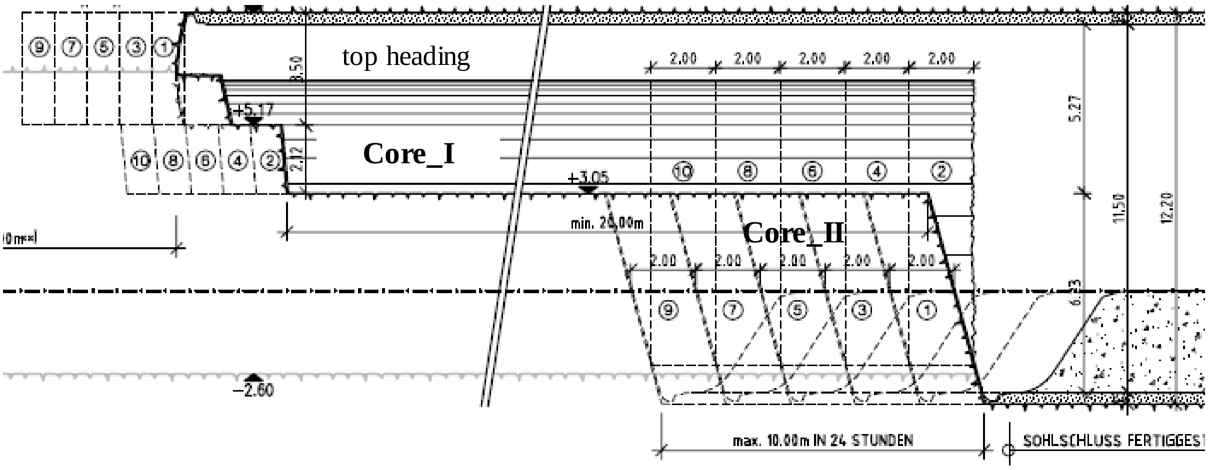

Figure 5.8: Excavation procedure of Core_II

5.2.5 Trial field plan

Figure 5.9 shows the arrangement of trial field together with the stations (Tunnel Meters: TM). The GFK trial field ranges from TM 50 to TM 100. The ground surface settlements measurements from the points at TM 64 and TM 86 are used to compare with the numerical results. The points for geotechnical instrumentation at this tunnel section are shown in Figure 5.10(a). Similar points are chosen in the mesh for the numerical analysis (Figure 5.10(b)).

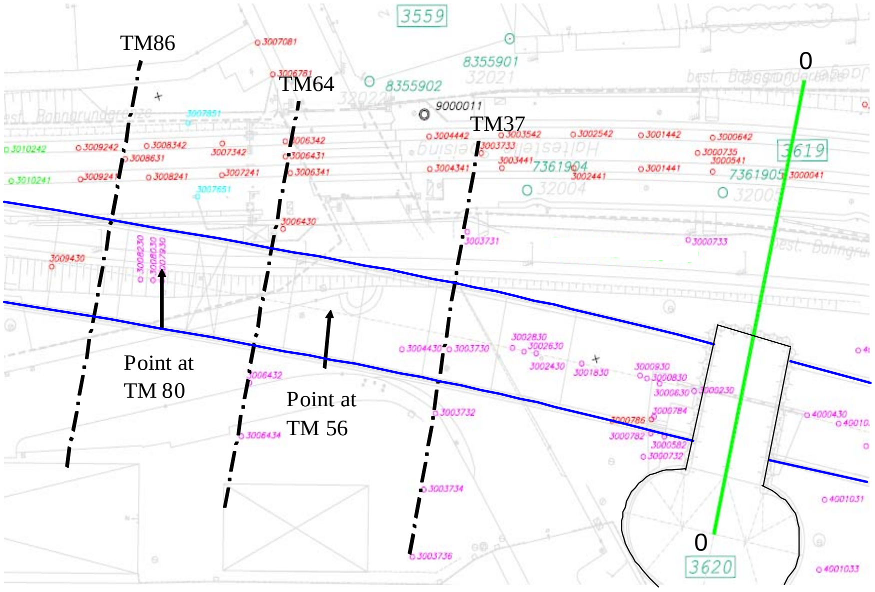

Figure 5.9: Settlement survey gird at the trial field

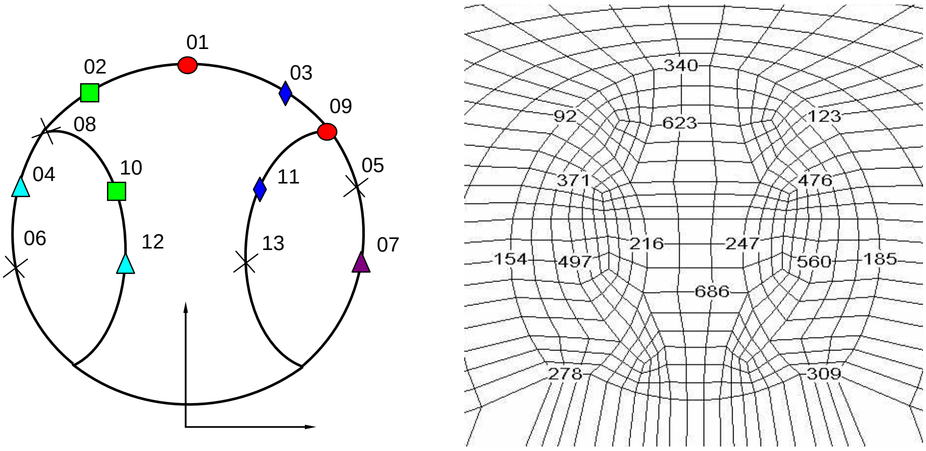

(a) (b)

Figure 5.10: Points of measurements in tunnel cross section: (a)Points for geotechnical instrumentation, (b) Points in numerical model

5.3 Numerical Simulation

5.3.1 Numerical model

Since the excavation procedure is not symmetric, we could not take advantage of geometrical symmetry. Therefore the mesh for the whole tunnel section is generated. A tunnel length of 90 m is considered. The top of tunnel is located about 21.5 m below the ground surface. The coordinate system is defined with the origin at the bottom of the tunnel; the z-axis points upward and the y-axis points along the axis of tunnel. The finite difference code FLAC3D is used for our calculations. The finite difference grid is shown in Figure 5.11. The input parameters of the hypoplasstic model are given in Table 5.3. The parameters are determeined from the soil properties obtained from numerous laboratory tests (see Table 5.1). Considering the diffrenece between the laboratory condidtions and the jobsite, the elastic modulus used in the simulation is about 60 % of its laboratory result.

Table 5.3: Material parameters used in the simulation

E [MPa]	μ [-]	ψ [°]	ϕ [°]	c [kPa]
25	0.4	5	23	60

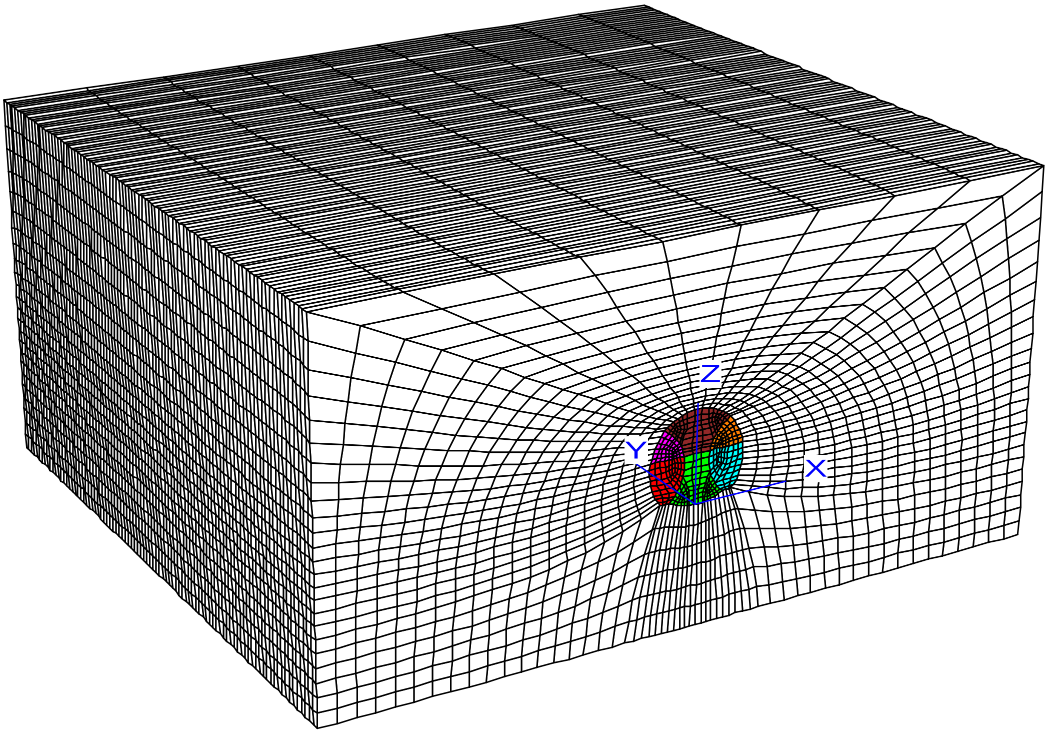

Figure 5.11: Finite difference grid of tunnel model

5.3.2 Simulation of sequential excavation

As is usual practice in NATM, the excavation and support are carried out sequentially. The face advancing is divided into four phases, namely (a): left side gallery drift, (b): right side gallery drift, (c): Core_I advance and (d): Core_II advance. The longitudinal distance between each face advancing is required not to be less than 20 m. The advancing procedure and support measures in longitudinal direction are the same for both side galleries.

It is noticed that the calculation time for using the hypoplastic model is about two times of it for using the Morh-Coulomb model in the simulation of excavation and support for a shallow tunnel described in Chapter 4. For avoiding long lasting calculations in this simulation, a fast way of simulation steps is developed. There are two aspects of the fast way. One is that the cutlength of 10 m is used. The other is that the final surface settlement is caused by the side galleries advance, the Core_I advance and the Core_II advance([4]). The final surface settlement is obtained from suming these three parts. The calculation of the fast way took about 2 weeks same as the calculaiton time using the Mohr-Coulomb model with 1 m cutlength. The simulated steps are the following:

(1) Definition of the stress state prior to tunnel excavation by applying an initial stress filed. The horizontal stress is calculated according to the formula for the earth pressure coefficient at rest in soil mechanics: $K_0 = 1 - \sin\phi$;

(2) The left side gallery is advanced to 40 m. As shown in Figure 5.6, the excavation length of top heading, bench and invert are 1m, 1m and 2 m respectively. The shotcrete installation and the increase of stiffness with time are simulated using shell structural elements as shwon in Figure 5.12. The basic approach is that the shotcrete installation for top heading, bench and invert is always 1 m, 1 m and 2 m behind the corresponding excavation, bench and invert. And the strength of shotcrete starts with an elastic modulus of 5 GPa for the first two excavation rounds and is thereafter increased after each excavation round by 5 GPa till the final elastic modulus of 15 GPa;

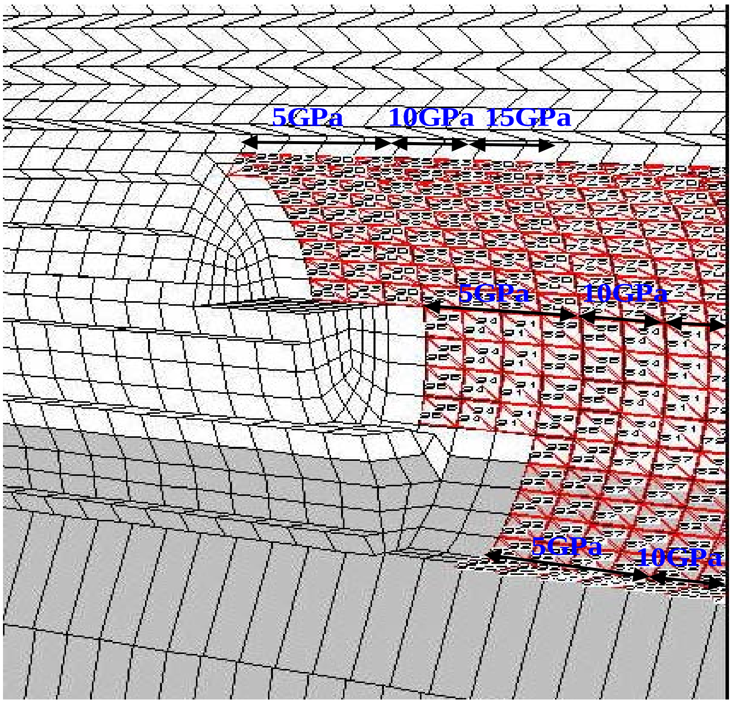

Figure 5.12: Simulation of installation of shotcrete at side galleries

(3) The right side gallery is advanced to 20 m. The excavation procedure of right side gallery is exactly same as the left side gallery. This applies to the shotcrete installation as well;

(4) The left side gallery is advanced to 60 m;

(5) The right side gallery is advanced to 40 m. The surface settlement caused by

the side galleries can be obtained after this simulation step;

(6) The Core_I is advanced to 40 m after the right side gallery is advanced to 60 m. The surface settlement caused by the Core_I advance can be obtained after this simulation step. The horizontal glass fibre anchors are installed in this step after the Core_I is excavated 1 m. The shotcrete installation is 1 m behind of the excavation. The strength development of shotcrete is same as in side galleries. The GFK anchors are modelled using cable structural elements with the following properties (Table 5.4);

Table 5.4: Properties of the cable structural elements

E [GPa]	Cable area [m^2]	grout stiffness [N/m/m]	grout friction angle [°]	grout cohesive strength [N/m]	tensile strength [N/m]
40	4.8×10^{-4}	2×10^9	15.3	4×10^4	283×10^3

(7) The Core_II is advanced to 40 m after the Core_I is excavated to 60 m. The surface settlement caused by the Core_II advance can be obtained after this simulation step. In this simulation step, the removal of the shotcrete (inner wall) of the side galleries is followed after the excavation of the Core_II;

5.4 Numerical Results

5.4.1 Longitudinal deformation profile

The mumerical results and measurements of longitudinal deformation profiles are shown in Figure 5.13. The following observations can be made from Figure 5.13.

The undulations of the measured deformation profile are thought to reflect the advance stages of partial excavations, while the simulated profile does not show such undulations. The reason is believed that the fast way is used in the simulation. In general, the numerical results using hypoplastic model agree well with the measurements. A perusal of the numerical calculations with and without advancing face support shows that the effect on the surface settlement is minimal. It seems that the mobilization of the GFK anchors requires ground deformation to some extent. If the ground deformation is not large enough, the anchor force cannot be fully mobilized.

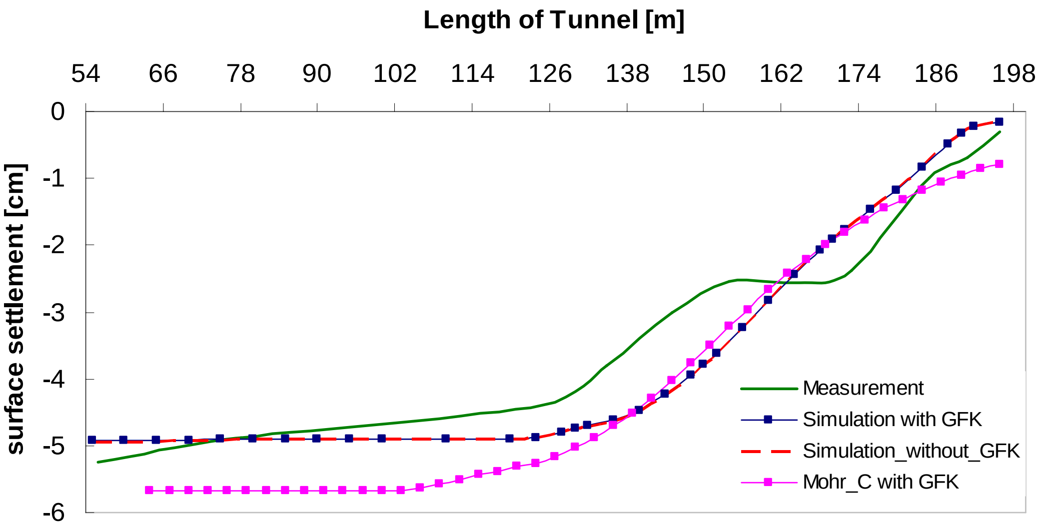

Figure 5.13: Comparison of longitudinal settlements between numerical results and measurements

In the above figure, the numerical results obtained from Mohr-Coulomb model are also provided ([4], [18]). Comparing the numerical results from these two models, it is apparent that the hypopalstic model provides more satisified longitudinal settlements profile.

5.4.2 Transversal settlement trough

The ground surface settlements at TM64 and TM84 are measured when the tunnel advance stage reaches 178_167_142_120 (the excavation of left side gallery is at TM178, the right side gallery is at TM167, the excavation of Core_I is at TM142, the excavation of Core_II is at TM120). It is clear that Core_II has been excavated far enough from the trial field, so the settlements at the trial field can be considered as in a steady state.

The calculated and measured settlement troughs at two tunnel stations TM64 and TM86 are shown in Figure 5.14. As can be seen from Figure 5.14, there is only minor difference between the calculated surface settlements at TM64 and TM86. This is ascribed to the fact that Core_II has been excavated far enough and the ground surface deformation at these two stations has reached a steady state. This agrees well with the observations made at the trial field. Comparing the numerical with the measured data shows that the maximal settlements are well predicted. However, the settlement troughs predicted by the hypoplastic model are much wider than the

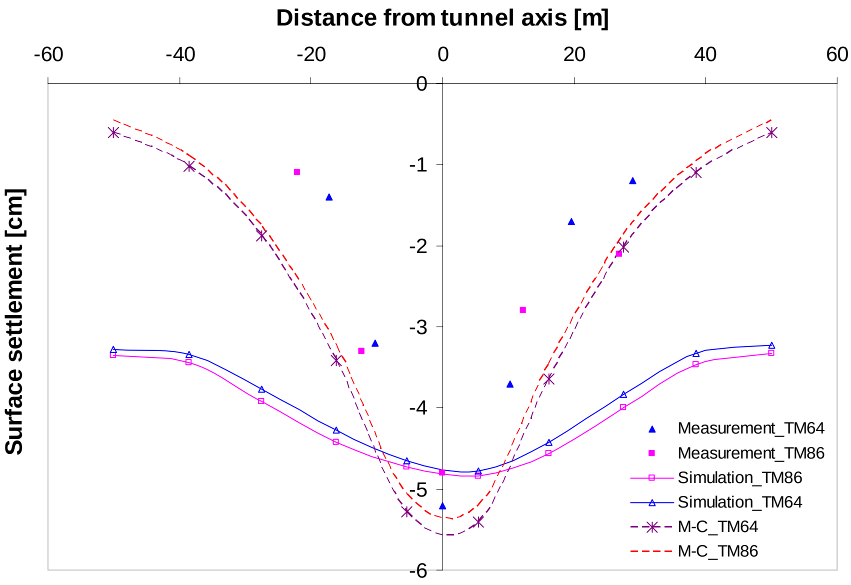

Figure 5.14: Comparison of transversal troughs between numerical results and measurements

measured. Comparing the transversal settlement troughs obtained from the hypoplastic model and Morh-Coulomb model, it can be seen that the width of settlement troughs predicted by the hypopalstic model is aslo larger that it predicted by Mohr-Coulomb model.

5.5 Discussion

Based on the previous section, It is noticed that the surface settlement at 50 m from the tunnel axis using the hypopalstic model is still about 3 cm (Figure 5.14). The surface settlement troughs predicted by the hypoplastic model are wider than those obtained from Mohr-Coulomb model and even much wider than the measurements. This can be explained by the following study based on a circular tunnel with a diameter of 12 m. The excavation is simulated by the hypoplastic model and Mohr-Coulomb model. Figure 5.15 shows the model grid of the circular tunnel in FLAC3D. By making use of the symmetry, only half of the tunnel is modelled. The model of the circular tunnel is 100 m wide, 54 m high and 100 m long. The overburden of the tunnnel is 21 m. The material parameters are given in Table 5.5.

Table 5.5: Material parameters for the circular tunnel

E [MPa]	μ [-]	ψ [°]	ϕ [°]	c [kPa]
40	0.4	5	23	60

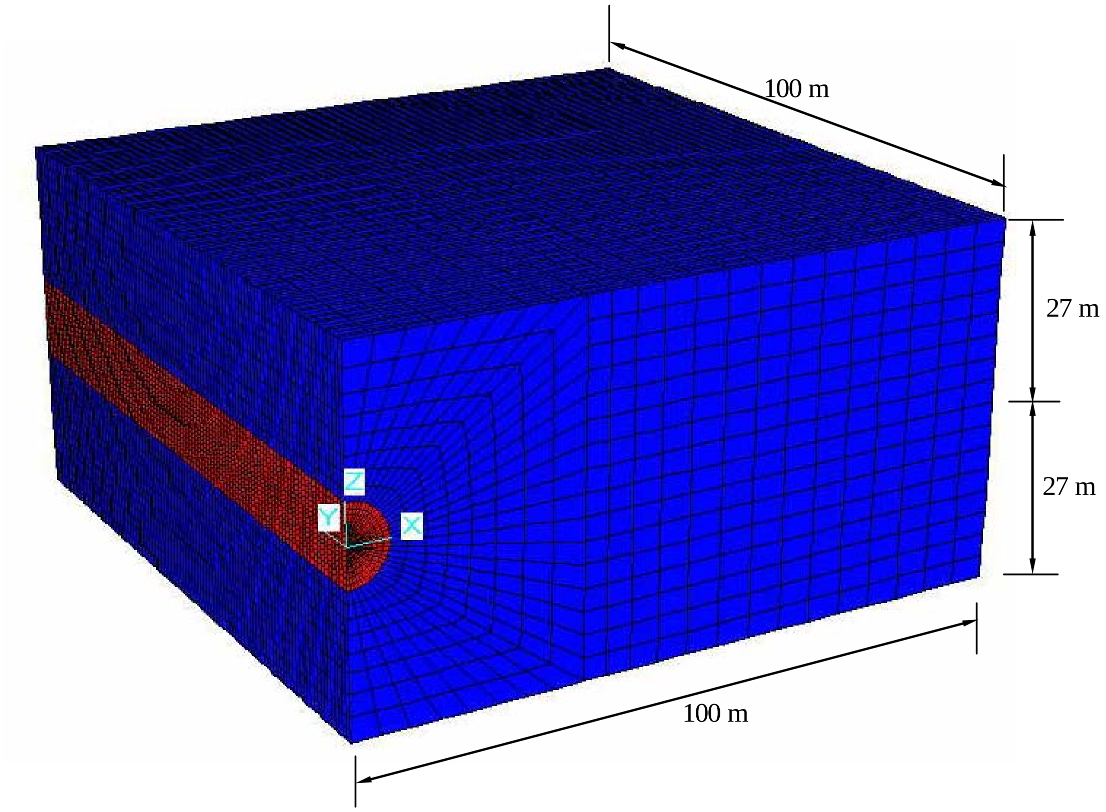

Figure 5.15: Model grid of the circular tunnel

Because of the objective of this study, no support is considered in the simulation. The model is subjected to an inital in-situ gravitational loading. The excavation is conducted incrementally with a cutlength of 1 m till it reaches 20 m from the portal.

The following figure shows the numerical results of the transversal settlement troughs. The settlements trouhgs of two tunnel cross sections are provided, i.e. TM2 and TM5.

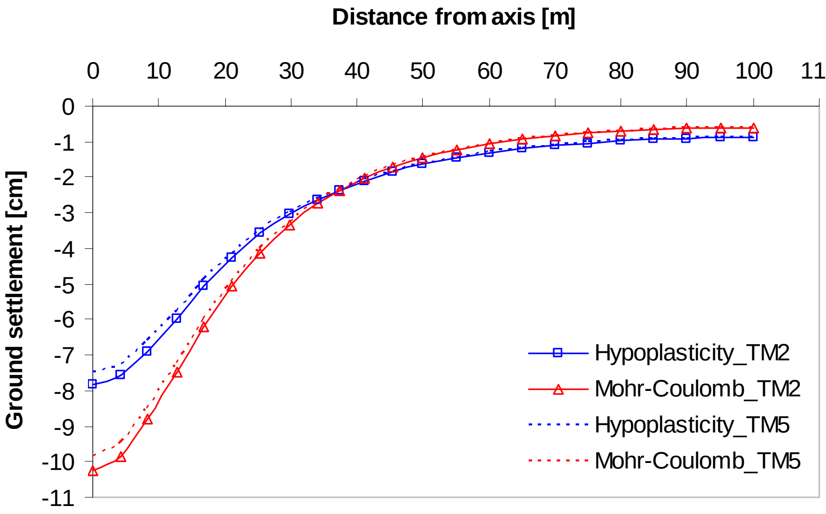

Figure 5.16: Numerical results of the transversal settlement troughs

From the calculated data shown in Figure 5.16, it can be seen that the surface settlements at 50 m from the axis are still about 2 cm for both models. The surface settlements at about 70 m from the axis reduces to about 10 % of the maximum surface settlement (above the tunnel axis). Based on this result, the model width for a tunnel with 12 m height should be not less than 70 m at least so that the effect of the boundaries on the transversal surface settlement troughs remains to be small (less than 10 %). In the simulation of Lainzertunel, the width of the FLAC3D model for the Lainzer tunnel is only 50 m. This offers an explanation for the wide settlement troughs with the hypoplastic model.

The settlement troughs are usually determined by empirical methods in practice. We known that the width of surface settlement troughs based on the empirical method is determined by the distance from the tunnel axis to the inflection point i (as Figure 5.17 shown). From the calculated data shown in Figure 5.16, the horizontal distance from the axis to the inflection point i obtained from the hypoplastic model is about 20 m as for the from Mohr-Coulomb model. As Peck (1969) ([15], [14]) suggested, the horizontal distance from the axis to the inflection point i is related to the tunnel depth and the tunnel diameter. From the numerical results in Figure 5.16, it can be seen that for tunnels with 12 m diameter and 21 m overburden, the horizontal distance from the axis to the inflection point i is about 20 m. Back to the numerical results for the Lainzer tunnel (Figure 5.14), the transversal troughs predicted by the Mohr-Coulomb model is about 20 m, however the hypopalstic model did not show such agreement. This can be explained by the simulated excavation procedure. In the simulation of

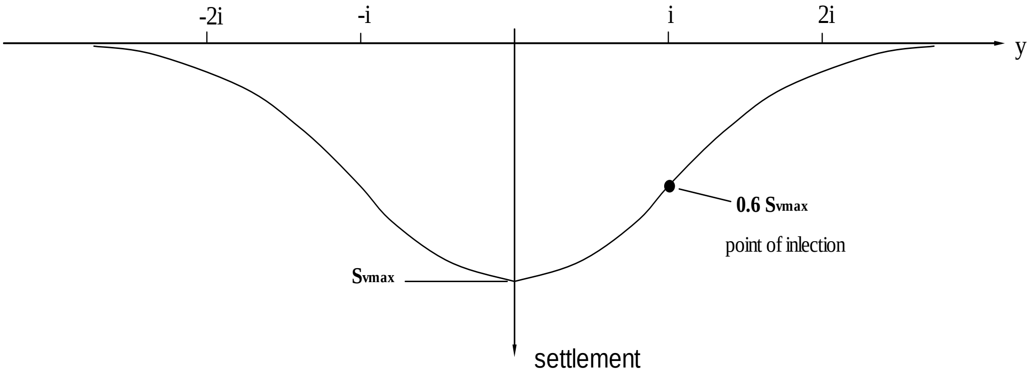

Figure 5.17: Gaussian curve for the transveral settlement trough

Lainzer tunnel, the cutlength of 1 m is used for the Mohr-Coulomb model, however when using the hypoplastic model, a cutlength of 10 m is used to save calculation time. This is thought to be responsible for the wider settlement troughs obtained with the hypoplastic model. The hypoplastic model generally leads to more calculation time. An optimisation of the numerical integration of the constitutive model is desirable.

Chapter 6

Conclusions and recommendations

This thesis traces the research into numerical implementation and application of an updated hypoplastic constutitive model. The updated hypoplastic model introduced a new term based on a simple hypoplastic model by Wu and Bauer (1994), which shows excessive contraction (volume reduction) in triaxial extension. In this updated model, critical state can be reached for all deviatoric stress paths. Moreover, cohesion is taken into account by using a translated stress.

The updated hypoplastic constitutive equation has been successfully implemented into the finite difference code FLAC3D. The implementation is verified by simulating some laboratory tests, i.e. isotropic compression test, triaxial tests, biaxial tests and simple shear tests. The numerical results of these tests are corroborated by numerical tests with one element.

Afterwards the hypoplastic model is used to simulate the excavation and support of shallow NATM tunnels. The excavation and support for a shallow tunnel from FLAC3D handbook is simulated using the updated hypoplastic model. Comparing with the Mohr-Coulomb model, the hypoplastic model predicts similar longitudinal troughs and the differences of longitudinal troughs between the two models are very small. Sa to transverse troughs, the hypopalstic model gives rise to wider settlement troughs than the Mohr-Coulomb model and the hypoplastic model predicted wider transverse troughs than the Mohr-Coulomb model.

The updated hypoplastic model is further applied to model a shallow NATM tunnel in Vienna urban area construction. The numerical results of the longitudinal surface settlements obtained from the hypolastic model agree well with the measurements, while the transversal settlement troughs are wider than the measurements.

In this updated hypoplastic model, only the small number of material parameters are introduced, obviously it does not allow us to tune the model predictions in great detail. For further research, the following modifications for the updated hypoplastic model can be considered:

- Incorporate void ratio into the model. The motivation lies in the history dependence in the model. Some experiments in the literature shows that both the stress ratio and the void ratio approach the critical state asympotically under increasing deformation.
- Introduce a second-order gradient of the strain rate into the model. The strain-gradient extension is aimed at the adquate modelling of the shear band formation in the post-localization regime.

Bibliography

[1] Bardet, J.P. Lode dependences for isotropic pressure-sensitive elastoplastic materials, J.Appl. Mech., ASME, 57: 498-506, 1990.

[2] Bauer, E. Calibration of a comprehensive constutitive model for granual materials, Soils and foundations, 36: 13-26, 1996.

[3] Bauer, E. Constutive modelling of critical states in hypoplasticity, Proc. of the fifth Int. Symp. on Numerical Models in Geomechanics-NUMOG , Davos, Switherland, Balkema, 6-8,Sep. 1995.

[4] Bauer, J. Numerical analysis of shallow NATM tunnel with face support by horizontal glass fibre dowels, DIPLOMARBEIT NR.336, Institut fr Geotechnik, Universitt Bodenkultur, 2008.

[5] Wang, C.C. A new representation theorem for isotropic functions, part I and part II. *J. Rat. Mech. Anal.*, 36, 166 - 223, 1970

[6] Itasca Consulting Group, Inc. *FLAC3D* (Fast Lagrangian Analysis of Constinua in 3 Dimensions),Version 3.0. Minneapolis, MN 55401, 2005.

[7] Kolymbas, D. A rate-dependent constitutive equation for soils. *Mech. Res. Comm.*, 4:367-372, 1977

[8] Kolymbas, D. A genrealized hypoelastic constitutive law. In *Proc.XI Int.Conf. Soil Mechanics and Foundation Engineering*, Vol.5, p2626, 1985.

[9] Kolymbas, D. A novel constitutive law for soils. *Second Int. Conf. on Constitutive Laws for Engineering Materials: Theory and Applications, Tuscon, Arizona,* Elsevier, January 1987.

[10] Kolymbas, D. An outline of hypoplasticity, Arch. Appl. Mech., 61: 143-151, 1996.

[11] Kolymbas, D. (Editor) Constitutive Modelling of Granular Materials, Springer, 1999.

[12] Lade, P.V. and Duncan, J.M. Elastoplastic stress-strain theory for cohesionless soil, *J. Geotech. Eng. Div.*, ASCE, 101:1037-1053, 1975.

[13] Matsuoka, H and Nakai, T. Stress deformaion and strength characteristics soil under three different principal stress, *Proc. Janpanese Soci. Civil Eng.*, 232:59-70, 1974.

[14] Moeller, S. Tunnel induced settlements and structural forces in linings, Mitteilung 54 des Instituts fr Geotechnik, Universitt Stuttgart, 2006.

[15] Peck, R. B. Deep excavation and tunnelling in soft ground. In *7th int. conference on Soil Mechanics and Foundation Engineering*,Sociedad Mexican de Mecanica de Suelos, A.C., 225-290, 1969.

[16] Tanseng, P. Implementation of Hypoplastic for Fast Largrangian Simulations, Verlag Berlin, 2005.

[17] von Wolffersdorff, P.-A. A hypoplasttic relation for granual materials with a predefined limit state surface, *Mechanics of Cohesive-Frictional Materials*, 1:251-271,1996.

[18] Wang, X.T., Wu, W. and Bauer, J. 3D numerical analysis of a shallow NATM tunnel with advancing face support by horizontal glass fibre anchors, *The first International Symposium on Computational Geomechanics* (ComGeo I), Juan-les-Pins, Cote d'Azur, France, April 29th - May 1st, 2009.

[19] Wang, X.T., Wu, W. and Tejchman, J. Update a hypoplastic constitutive model, Proc. of 36th Solid Mechanics Conference, Gdansk, Poland, 206, Sep. 9-12, 2008.

[20] Wu, W. Hypoplastizität als mathematisches Modell zum mechanischen Verhalten granularer Stoffe. *Pulication Series of the Institute of Soil Mechanics and Rock Mechanics, No. 129, Karlsruhe University*, 1992.

[21] Wu, W. On a simple critical state model for sand, Proc. of the seventh Int. Symp. on Numerical Models in Geomechanics-NUMOG , Graz, Austria, Balkema, 47-52, 1999.

[22] Wu, W. and Bauer, E. A simple hypoplastic constitutive model for sand, Int. J. Numer. Anal. Methods Geomech., 18: 833-862, 1994

[23] Wu, W., Bauer, E., Kolymbas, D. Hypoplastic constitutive model with critical state for granular materials, Mechanics of Materials, 23:45-69, 1996.

[24] Wu, W. and Kolymbas, D. Numerical testing of the stability critierion for hypoplastic constitutive equations, Mech. Mater., 9:245-253, 1990.

[25] Wu, W. and Kolymbas, D. Hypoplastic then and now. In D. Kolymbas, editor, *Constitutive Modelling of Granular Material.* Springer, 2000.

[26] Wu, W. and Niemunis, A. Beyond invertibility surface in granular materials, Localisation and Bifurcation Theory for Soils and Rocks, 113-126, 1994.

[27] Wu, W. and Niemunis, A. Failure criterion, flow rule and dissipation function derived from hypoplasticity, Mech. Coheisive-Frictional Mater., 1:145-163, 1996.

Appendix A

Implementation code of the updated hypoplastic model

```
# include ”userhypo2.h”
#include ”math.h”
static const double dPi = 3.14159265358979/180.0;
static const double D1D3 = 1.0/3.0;
static const double D2D3 = 2.0/3.0;
static UserHypoModel userhypomodel(true);
UserHypoModel::UserHypoModel(bool bRegister)
            :ConstitutiveModel(mnUserHypoModel,bRegister),
            dEE(0.0),dFriction(0.0),dDilation(0.0),dPoisson(0.0)
            ,dCohesion(0.0),dShear(0.0), dBulk(0.0),dC1(0.0),dC2(0.0)
            ,dC3(0.0), dC4(0.0) ,dMP(0.0), dMQ(0.0), dEV(0.0)
{
}
const char ∗UserHypoModel::Keyword(void) const  return(”userhypo2”);

const char ∗UserHypoModel::Name(void) const  return(”userhypoplasticity2”);

const char ∗∗UserHypoModel::Properties(void) const
{
  static const char ∗strKey[] =
  {
```

```
    ”young”, ”friction”, ”dilation”,”poisson”,”cohesion”,”shear”,
    ”bulk”,”Coe1”,”Coe2”,”Coe3”,”Coe4”, ”cp”,”cq”,”ev”,0
   };
   return(strKey);
}

const char ∗∗UserHypoModel::States(void) const
{
   static const char *strKey[] =
   {
   ”shear-n”,”tension-n”,”shear-p”,”tension-p”, 0
   };
   return(strKey);
}

double UserHypoModel::GetProperty(unsigned ul) const
{
   switch(ul)
    {
    case 1: return(dEE); // tangential modulus
    case 2: return(dFriction); // friction angle
    case 3: return(dDilation); //dilatancy angle
    case 4: return(dPoisson); //initial Poisson ratio
    case 5: return(dCohesion);
    case 6: return(dShear);
    case 7: return(dBulk);
    case 8: return(dC1);
    case 9: return(dC2);
    case 10: return(dC3);
    case 11: return(dC4);
    case 12: return(dMP); // mean effective stress
    case 13: return(dMQ); // second deviatoric stress
    case 14: return(dEV); // volumetric strain
   }
```

```
    return(0.0);
}

void UserHypoModel::SetProperty(unsigned ul, const double &dVal)
{
    switch (ul)
    {
    case 1: dEE = dVal; break;
    case 2: dFriction = dVal; break;
    case 3: dDilation = dVal; break;
    case 4: dPoisson = dVal; break;
    case 5: dCohesion = dVal; break;
    case 6: dShear = dVal; break;
    case 7: dBulk = dVal; break;
    case 8: dC1 = dVal; break;
    case 9: dC2 = dVal; break;
    case 10: dC3 = dVal; break;
    case 11: dC4 = dVal; break;
    case 12: dMP = dVal; break;
    case 13: dMQ = dVal; break;
    case 14: dEV = dVal; break;
    }
}

const char *UserHypoModel::Copy(const ConstitutiveModel ∗cm)
{
    const char ∗str = ConstitutiveModel::Copy(cm);

    if (str) return(str);
    UserHypoModel ∗hm = (UserHypoModel ∗)cm;
    dEE = hm→dEE;
    dFriction = hm→dFriction;
    dDilation = hm→dDilation;
    dPoisson = hm→dPoisson;
```

```
    dCohesion = hm→dCohesion;
    dShear = hm→dShear;
    dBulk = hm→dBulk;
    dC1 = hm→dC1;
    dC2 = hm→dC2;
    dC3 = hm→dC3;
    dC4 = hm→dC4;
    dMP = hm→dMP;
    dMQ = hm→dMQ;
    dEV = hm→dEV;
    return(0);
}

const char *UserHypoModel::Initialize(unsigned uDim, State *)
{
    if ((uDim!=3)&&(uDim!=2))
    return (”Illegal dimension in user-defined hypoplastic model”);
//   Get the coefficient; C1, C2, C3, C4;
//   double dC1,dC2,dC3,dC4;
    double Ksf, Kei, Kef, Ldi, Ldf;
    double Cof_u, C2part1,C2part2,C2part3;
    double C3part1, C3part2, C3part3;

    Ksf = (1+sin(dFriction * dPi))/(1-sin(dFriction * dPi));
    Kei = dPoisson;
    Kef = (1+tan(dDilation * dPi))/2.0;
    Ldi = sqrt(1+2.0 * Kei*Kei);
    Ldf = sqrt(1+2.0 * Kef*Kef);

    double ff=(Ksf-2.0 * Kef)/(2.0 + Ksf);
    Cof_u = (1+Kei)*(2.0*Kei-1.0)*(Ksf-1.0)*
     (-1.0 + 2.0 * Kef + 3.0 * ff)*Ldf;
// Get the coefficient C1
    dC1 = -dEE/((3.0 + 3.0 * Kei)*100000); // 100kPa –confining pressure
```

```
// Get the coefficitent C2
 C2part1 = (-1.0 + 2.0 * Kef - Kef * Ksf + 2.0 * Kef*Kef*Ksf);
 C2part2 = (4.0 - 5.0*Kei -2.0*Kef - 2.0*Kei*Kef);
 C2part3 = -1.0 - Kei + 5.0*Kef - 4.0*Kei*Kef;
dC2 = dEE*(3.0*Ldi*C2part1+Ldf*C2part2+Ksf*Ldf*C2part3)/(100000*Cof_u);
// Get the coefficient C3
 C3part1 = -2.0 + 4.0*Kei + Kef - 2.0 * Kei*Kef;
 C3part2 = 1.0 - 2.0*Kei - 5.0*Kef + 10.0*Kei*Kef;
 C3part3 = Ldi + Kef*Ksf*Ldi - Kei*Ldf + Kei*Ksf*Ldf;
dC3 = dEE*(2.0*Ldf*C3part1+Ksf*Ldf*C3part2+
      9.0*ff*C3part3)/(3*100000*Cof_u);
// get the coeeficient C4
   dC4 = 3.0 * dC1 * (Kef*Ksf+1)/(Ldf*(Ksf-1));
   return(0);
}

static const int Qav =0;
static const int Evav =1;
static const int Pav =2;
const char *UserHypoModel::Run(unsigned uDim, State *ps)
{
   if ((uDim!=3)&&(uDim!=2))
   return ("Illegal dimension in user-defined hypoplastic model");

// initialize stacks
   if (ps→bySubZone==0)
   {
   ps→working[Qav] =0.0;
   ps→working[Evav]=0.0;
   ps→working[Pav] =0.0;
   }

   int iPlas = 0;
//——— trial stresses——
```

```
    double dE11 = ps→stnE.d11; // stnE—-strain increment tensor
    double dE22 = ps→stnE.d22;
    double dE33 = ps→stnE.d33;
    double dE12 = ps→stnE.d12;
    double dE13 = ps→stnE.d13;
    double dE23 = ps→stnE.d23;
    double diS11 = ps→stnS.d11; // stnS—-stress tensor
    double diS22 = ps→stnS.d22;
    double diS33 = ps→stnS.d33;
    double diS12 = ps→stnS.d12;
    double diS13 = ps→stnS.d13;
    double diS23 = ps→stnS.d23;
    double trT; // tr(stress)
    double trD; // tr(strain increment)
    double trTD; // tr(stress * strain increment)
    double trT_3; // (tr(stress))/3.0;
    double DD;
    double trTD_trT;
    double dS11 = diS11 - dCohesion;
    double dS22 = diS22 - dCohesion;
    double dS33 = diS33 - dCohesion;
    double dS12 = diS12;
    double dS13 = diS13;
    double dS23 = diS23;

    trT = dS11 + dS22 + dS33;
    trD = dE11 + dE22 + dE33;
    trTD = dS11 * dE11 + dS22 * dE22 + dS33 * dE33 +
     2.0 * dS12 * dE12 + 2.0 *dS13 * dE13 + 2.0 * dS23 * dE23;
    trT_3 = trT/3.0;
    trTD_trT = trTD / trT;

  // ||strain increment||
    DD = sqrt(dE11*dE11 + dE22*dE22 + dE33*dE33
```

```
    + 2.0*dE12*dE12 +2.0*dE13*dE13+ 2.0*dE23*dE23 ) ;

// deviatoric stress tensor
   double dDS11 = dS11 - trT_3;
   double dDS22 = dS22 - trT_3;
   double dDS33 = dS33 - trT_3;
   double dDS12 = dS12 ;
   double dDS13 = dS13 ;
   double dDS23 = dS23 ;

// second deviatoric stress
   double dJ2 = (0.5)*(dDS11*dDS11+ dDS22*dDS22+dDS33*dDS33)+
    ps→stnS.d12 * ps→stnS.d12 + ps→stnS.d23 * ps→stnS.d23
    + ps→stnS.d13 * ps→stnS.d13;
   double dQval = sqrt(3.0*dJ2);

// volumetric strain
   double dEVval = (ps→stnE.d11 + ps→stnE.d22 + ps→stnE.d33);
// mean pressure
   double dPval = -(dS11 + dS22 + dS33)*D1D3;

// increment of stress
   double dS11a, dS11b, dS11c, dS11d;
   double dS22a, dS22b, dS22c, dS22d;
   double dS33a, dS33b, dS33c, dS33d;
   double dS12a, dS12b, dS12c, dS12d;
   double dS13a, dS13b, dS13c, dS13d;
   double dS23a, dS23b, dS23c, dS23d;
   double incrS11, incrS22, incrS33, incrS12, incrS13, incrS23;

   dS11a = dC1 * trT * dE11;
   dS11b = dC2 * trTD_trT * dS11;
   dS11c = dC3 * trD * dS11;
   dS11d = dC4 * (dS11 + dDS11) * DD;
```

```
    incrS11 = dS11a + dS11b + dS11c + dS11d;

    dS22a = dC1 * trT * dE22;
    dS22b = dC2 * trTD_trT * dS22;
    dS22c = dC3 * trD * dS22 ;
    dS22d = dC4 * (dS22 + dDS22) * DD;
    incrS22 = dS22a + dS22b + dS22c + dS22d;

    dS33a = dC1 * trT * dE33;
    dS33b = dC2 * trTD_trT * dS33;
    dS33c = dC3 * trD * dS33;
    dS33d = dC4 * (dS33 + dDS33) * DD;
    incrS33 = dS33a + dS33b + dS33c + dS33d;

    dS12a = dC1 * trT * dE12;
    dS12b = dC2 * trTD_trT * dS12;
    dS12c = dC3 * trD * dS12;
    dS12d = dC4 * (dS12 + dDS12) * DD;
    incrS12 = dS12a + dS12b + dS12c + dS12d;

    dS13a = dC1 * trT * dE13;
    dS13b = dC2 * trTD_trT * dS13;
    dS13c = dC3 * trD * dS13;
    dS13d = dC4 * (dS13 + dDS13) * DD;
    incrS13 = dS13a + dS13b + dS13c + dS13d;

    dS23a = dC1 * trT * dE23;
    dS23b = dC2 * trTD_trT * dS23;
    dS23c = dC3 * trD * dS23;
    dS23d = dC4 * (dS23 + dDS23) * DD;
    incrS23 = dS23a + dS23b + dS23c + dS23d;

// update the stresses
    ps→stnS.d11 += incrS11;
```

```
    ps→stnS.d22 += incrS22;
    ps→stnS.d33 += incrS33;
    ps→stnS.d12 += incrS12;
    ps→stnS.d13 += incrS13;
    ps→stnS.d23 += incrS23;
    double dVol = ps→dSubZoneVolume;
    ps→working[Qav] += dQval * dVol;
    ps→working[Evav] += dEVval * dVol;
    ps→working[Pav] += dPval * dVol;

// the last zone has been processed
    if (ps→bySubZone==ps→byTotSubZones-1)
    {
    dVol = 1.0 / ps→dZoneVolume;
    if (ps→byOverlay ==2) dVol *=0.5;
    ps→working[Qav] = ps→working[Qav] * dVol;
    ps→working[Evav] = ps→working[Evav] * dVol;
    ps→working[Pav] = ps→working[Pav] * dVol;
    dMQ = ps→working[Qav];
    dEV += ps→working[Evav];
    dMP = ps→working[Pav];
    }
    Axes aDir;
    double dPrinMin, dPrinMid, dPrinMax, sdif=0.0, psdif=0.0;
    int icase=0;
    bool bFast=→stnS.Resoltopris(&dPrinMin, &dPrinMid,&dPrinMax,
    &aDir, uDim, &icase,&sdif, &psdif);
    double dPrinMinCopy = dPrinMin;
    double dPrinMidCopy = dPrinMid;
    double dPrinMaxCopy = dPrinMax;

    if(iPlas)
    {
    ps→stnS.Resoltoglob(dPrinMin, dPrinMid, dPrinMax,aDir,
```

```
     dPrinMinCopy,dPrinMidCopy,dPrinMaxCopy, uDim,
     icase, sdif, psdif, bFast);
    ps→bViscous = false; //inhibit stiffness-damping terms
    }
    else
    {
    ps→bViscous = true; // allow stiffness-damping terms
    }
    return(0);
}

// Save properties
const char *UserHypoModel::SaveRestore(ModelSaveObject *mso)
{
    const char *str = ConstitutiveModel::SaveRestore(mso);
    if(str) return(str);
    mso→Initialize(14,0);
    mso→Save(0,dEE);
    mso→Save(1,dFriction);
    mso→Save(2,dDilation);
    mso→Save(3,dPoisson);
    mso→Save(4,dCohesion);
    mso→Save(5,dShear);
    mso→Save(6,dBulk);
    mso→Save(7,dC1);
    mso→Save(8,dC2);
    mso→Save(9,dC3);
    mso→Save(10,dC4);
    mso→Save(11,dMP);
    mso→Save(12,dMQ);
    mso→Save(13,dEV);
    return(0);
}
//EOF
```